CHALMERS
UNIVERSITY OF TECHNOLOGY

Joint Localization, Synchronization and Mapping via Phase-Coherent Distributed Arrays

Citation for the original published paper (version of record):

Fascista, A., Deutschmann, B., Keskin, M. et al (2025). Joint Localization, Synchronization and Mapping via Phase-Coherent Distributed Arrays. IEEE Journal on Selected Topics in Signal Processing, 19(2): 412-429. http://dx.doi.org/10.1109/JSTSP.2025.3533111

(article starts on next page)

Joint Localization, Synchronization and Mapping via Phase-Coherent Distributed Arrays

Alessio Fascista, *Member, IEEE*, Benjamin J. B. Deutschmann, *Member, IEEE*, Musa Furkan Keskin, *Member, IEEE*, Thomas Wilding, *Member, IEEE*, Angelo Coluccia, *Senior Member, IEEE*, Klaus Witrisal, *Senior Member, IEEE*, Erik Leitinger, *Senior Member, IEEE*, Gonzalo Seco-Granados *Fellow, IEEE*, Henk Wymeersch, *Fellow, IEEE*

***Abstract*—Extremely large-scale antenna array (ELAA) systems emerge as a promising technology in beyond 5G and 6G wireless networks to support the deployment of distributed architectures. This paper explores the use of ELAAs to enable joint localization, synchronization and mapping in sub-6 GHz uplink channels, capitalizing on the near-field effects of phase-coherent distributed arrays. We focus on a scenario where a single-antenna user equipment (UE) communicates with a network of access points (APs) distributed in an indoor environment, considering both specular reflections from walls and scattering from objects. The UE is assumed to be unsynchronized to the network, while the APs can be time- and phase-synchronized to each other. We formulate the problem of joint estimation of location, clock offset and phase offset of the UE, and the locations of scattering points (SPs) (i.e., mapping). Through comprehensive Fisher information analysis, we assess the impact of bandwidth, AP array size, wall reflections, SPs and phase synchronization on localization accuracy. Furthermore, we derive the maximum likelihood (ML) estimator for the joint localization, synchronization, and mapping problem, which optimally combines the information collected by all the distributed arrays. To overcome its intractable high dimensionality, we propose a novel three-stage algorithm that first estimates phase offset leveraging carrier phase information of line-of-sight (LoS) paths, then determines the UE location and clock offset via LoS paths and wall reflections, and finally locates SPs using a null-space transformation technique. Simulation results demonstrate the effectiveness of our approach in distributed architectures supported by radio stripes (RSs) — an innovative alternative for implementing ELAAs — while revealing the benefits of carrier phase exploitation and showcasing the interplay between delay and angular information under different bandwidth regimes.**

***Index Terms*– Extremely large-scale antenna arrays, distributed architectures, radio stripes, positioning, phase synchronization, carrier phase.**

I. Introduction

Different generations of wireless communication systems have boosted communication rates by essentially harnessing two orthogonal dimensions: frequency [1] and space [2], [3]. In terms of frequency, larger bandwidth available at increasingly higher carrier frequencies brought commensurate surges in capacity, motivating the transition from sub-6 GHz to mmWave in 5G [4], and the exploration of sub-THz in 6G [5]. In terms of space, larger antenna arrays provide spatial multiplexing and diversity gains, thus increasing either rate or reliability. This spurred the introduction of multiple-input-multiple-output (MIMO) in 3G-4G [6], leading to massive MIMO in 5G, and now extremely large-scale antenna array (ELAA) in 6G [7]. The increase in both bandwidth and antenna sizes led not only to improvements in data rates, but also, first as a side-effect and now as a key service for 6G, improvements in radio localization [8].

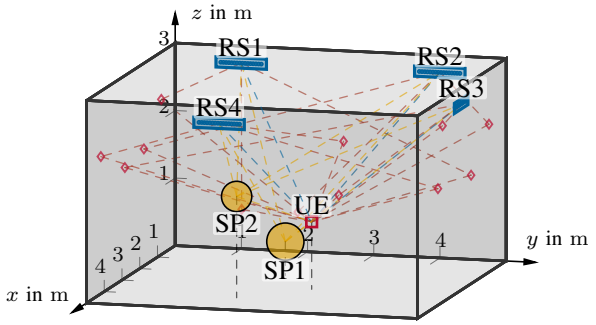

Fig. 1. Representative scenario of uplink user equipment (UE) localization supported by a network of $N = 4$ distributed radio stripes. There are $J = 2$ dominant scatterers, 4 walls, and a single UE.

The potential of such innovations for the sake of localization is primarily linked to the high resolution brought in the delay/distance domain via the bandwidth and in the angle domain via the array size [9], [10]. Combined, this resolution unleashes extreme accuracies in support of demanding 6G use cases such as extended reality, cooperating robots, and digital twins [11]. At the same time, due to the large bandwidth and apertures, conventional channel models were no longer appropriate, and effects such as wavefront curvature and channel non-stationary must be properly modeled to reap the full benefits [12].

Despite initial excitement about sub-THz bands, the reality is that mainly lower bands will support the bulk of 6G traffic [13]. This has put more focus on localization using ELAA systems with limited bandwidths. Such systems can be realized in various forms, such as a *physically large collocated antenna array*, *reconfigurable intelligent surface (RIS)*, *distributed arrays* or *radio stripes (RSs)* [7]. Among cell-free implementation alternatives, the RSs technology holds great potential as a cost-efficient distributed architecture for dense area deployments, such as stadiums, railway stations, within trains, and at public spaces [14]–[16], with applications involving communication [14], power transfer [17], and positioning. RSs are a distributed massive MIMO technology invented in 2017 and patented in 2018 by Ericsson [18]. Serially connected RSs communicate with a central processing unit (CPU) via a shared bus that simultaneously provides synchronization and

This work is supported, in part, by the SNS JU project 6G-DISAC under the EU's Horizon Europe research and innovation Program under Grant Agreement No 101139130 and by the Swedish Research Council (VR) through the project 6G-PERCEF under Grant 2024-04390. The project has received funding from the European Union's Horizon 2020 research and innovation programme under grant agreement No 101013425 (Project "REINDEER"). The financial support by the Christian Doppler Research Association, the Austrian Federal Ministry for Digital and Economic Affairs and the National Foundation for Research, Technology and Development is gratefully acknowledged.

power supply [14]. Unlike stripe-like RISs [19], RSs can actively transmit and sample/process received signals. From the viewpoint of positioning and sensing, synchronization of distributed arrays has been experimentally shown to improve angle-of-arrival (AoA) estimation accuracy [20]. In general, the different realizations of ELAA systems vary mainly in terms of whether observations are available in element-space (i.e., at each antenna) or beam-space (i.e., projected into a lower-dimensional space), following the terminology from [21]. Research on localization can similarly be divided based on these different points of view [22].

In terms of large collocated arrays, [23] considers narrowband localization using a dynamic metasurface antenna array, exploiting only the wavefront curvature in beam-space. A related problem is tackled in [24], considering again narrowband beam-space observations, but also accounting for multipath propagation. A far from exhaustive list of RIS-based works includes [19], [22], [25], [26]. Finally, distributed arrays, comprising many phase-coherent access points (APs) provide an extremely large near-field region, which was harnessed in [27]–[31]. Specifically, the works [27]–[29] consider wideband element-space observations at mmWave, combining the benefits of a wide aperture with a high delay resolution. Unfortunately, such systems are impractical since (i) phase synchronization among distributed arrays at mmWave bands is extremely challenging due to hardware imperfections (e.g., phase noise and frequency errors) [32, Sec. 6.2.1] and (ii) location calibration at a fraction of the wavelength (which is $1\,\mathrm{cm}$ at $30\,\mathrm{GHz}$) is also extremely difficult. Localization using space angle (SA) measurements at distributed linear arrays was studied in [30] in the absence of phase synchronization between the arrays and without considering any specific frequency band. Surprisingly, there are only limited research activities on the very practical setting of distributed cell-free MIMO localization under realistic propagation conditions at lower bands. We note that this problem bears some resemblance to the carrier phase positioning problem [33]. Our previous work [31], which forms the basis of the current paper, considered the impact of phase-coherent and phase-incoherent operation on uplink positioning at sub-6 GHz in realistic channels exhibiting dense multipath components (DMCs) [34].

Starting from our preliminary analysis in [31], this study addresses the problem of uplink joint positioning, synchronization, and environment mapping using distributed radio stripes (RSs) at sub-6 GHz frequencies. Unlike [31] where only the line-of-sight (LoS) component per UE-RS link is considered in the channel model, this paper incorporates reflection points (RPs) and scatter points (SPs) into the channel model, which captures the propagation characteristics much more accurately. In doing so, we propose a comprehensive generative model that accounts for specular reflection, bistatic scattering and dense multipath components. We derive novel estimators and fundamental bounds under various settings, considering RSs' different levels of phase/time synchronization and diverse multipath characteristics in indoor sub-6 GHz environments. The main contributions are as follows:

(i) We investigate the problem of joint uplink positioning, synchronization and mapping with distributed RSs, considering the distinctive properties of sub-6 GHz operation, including phase and time synchronization capabilities [35], dense multipath environment [36], [37] and carrier phase (CP) exploitation. For this challenging scenario, we propose a detailed generative model that accounts for the peculiar characteristics of the channels over the distributed RS network and allows for computation of the theoretical lower bounds under various operational assumptions.

(ii) We derive the ML estimator for joint localization, synchronization, and mapping, which optimally combines signal observations collected at all RSs. Unlike [31], which proposes an algorithm for localization and synchronization in a simplified LOS-only scenario, we propose a novel three-stage algorithm for localization, synchronization and mapping. Through a convenient re-parameterization, we are able to obtain ML estimates of the channel amplitudes for all involved paths in closed form, thereby reducing the dimensionality of the estimation process. To make the estimation task feasible, we propose novel reduced-complexity estimation algorithms for the remaining parameters in three steps. First, we estimate the phase offset by leveraging CP information of LoS paths. Subsequently, this is used to determine an initial estimate of the UE location and clock offset through a suitable relaxed ML estimator. Finally, such initial estimates are exploited for low-complexity mapping of dominant scatterers in the environment.

(iii) We derive the Cramér-Rao lower bounds (CRLBs) on position, clock and phase offsets estimation, including mapping of SPs, both with and without exploiting CP information. Our investigation highlights the impact of multipath overlap on estimation performance. We carry out a detailed investigation of fundamental theoretical limits on positioning under a wide range of conditions, such as varying bandwidth regimes and RS aperture sizes. Unlike [31], which employs a simplified LoS-only channel model, our investigation relies on the proposed more realistic channel model incorporating RP and SP components, and thus provides valuable insights into practical RS deployments for 6G networks.

(iv) We carry out extensive simulation analyses to assess the performance of the proposed algorithms in terms of position, clock/phase offset and SPs estimation accuracy, as a function of the main system parameters and operating conditions.

Notations: Vectors and matrices are denoted by boldface lower-case and upper-case letters, respectively. Symbols $(\cdot)^{-1}$, $(\cdot)^{\mathsf{T}}$, $(\cdot)^{\mathsf{H}}$, and $(\cdot)^{\dagger}$ denote the inverse, transpose, conjugate transpose (hermitian), and left pseudoinverse, respectively. $j=\sqrt{-1}$ is the imaginary unit and we denote with $\Re\{\cdot\}$ and $\Im\{\cdot\}$ the real and imaginary part operators. As to numerical sets, $\mathbb{R}$ and $\mathbb{C}$ represent real and complex numbers sets, respectively. We use $\mathbb{B}=\{0,1\}$ to denote the binary set. $\mathrm{Toep}(\boldsymbol{x},\boldsymbol{x}^{\mathsf{H}})$ denotes a Hermitian Toeplitz matrix with the first column $\boldsymbol{x}$ and the first row $\boldsymbol{x}^{\mathsf{H}}$. $\mathrm{reshape}_{M,K}(\cdot)$ reshapes a vector into an $M\times K$ matrix. We use $\mathbf{0}_{M\times N}$ and $\mathbf{1}_{M\times N}$ to denote $M\times N$ matrices of all zeros and all ones, respectively. The identity matrix is $\mathbf{I}$, where the size is left implicit. We use $\boldsymbol{x}\sim\mathcal{CN}_N(\mathbf{0},\boldsymbol{M})$ if $\boldsymbol{x}\in\mathbb{C}^N$ is a complex normal (N-dimensional) vector with zero mean and (Hermitian) positive definite covariance matrix $\boldsymbol{M}\in\mathbb{C}^{N\times N}$. $\mathbb{E}[\cdot]$ denotes the expected value, $\|\cdot\|$ is the Euclidean norm of a vector, whereas $\odot$ and $\otimes$ stand for Hadamard and Kronecker products.

II. System Model

Consider an RSs network composed of N stripes, each consisting of M antennas, and a single UE equipped with a single antenna and communicating with the network through the uplink (UL) channel [15], [38]. We will address both cases of presence or absence of *phase synchronization* between the

UE and the RSs network. In the former case, phase coherence effectively turns the RSs network into a large multiple-antenna access point [14, Sec. 3.1], while the UE has an unknown *phase offset* δ_ϕ and unknown *clock offset* δ_τ with respect to the RSs network. Indeed, the proposed system leverages the entire network of RSs as a large-scale distributed array with NM antennas. Since in realistic deployment scenarios it is reasonable to install multiple RSs per wall, the system's scale can be easily increased to obtain an ELAA.

We assume that the wavefront of the signal transmitted by the UE is planar over each individual RS (i.e., individual RSs lie in the far-field of the UE). However, we do not assume a planar but spherical wavefront over the entire RS network due to a large aperture distributed over a wide area. That is, we use a planar wavefront model per RS but a spherical wavefront model for the whole RS network. Moreover, the RSs are deployed around a rectangle at a specific height, as depicted in Fig. 1. Each individual RS is placed at a known phase center position $\boldsymbol{p}_n^{\text{RS}} = [p_{n,x}^{\text{RS}}\ p_{n,y}^{\text{RS}}\ p_{n,z}^{\text{RS}}]^\mathsf{T}$ with known azimuth orientation β_n around the z-axis, which is measured counter-clockwise from the x-axis[1], while the UE is located at an unknown position $\boldsymbol{p} = [p_x\ p_y\ p_z]^\mathsf{T}$.

We consider a UL communication scenario where the UE transmits orthogonal frequency division multiplexing (OFDM) pilots $\boldsymbol{s} = [s_1\ \cdots\ s_K]^\mathsf{T} \in \mathbb{C}^{K\times 1}$ over K subcarriers with spacing Δ_f, e.g., sounding reference signal (SRS) for 5G new radio (NR) UL positioning [39], $\|\boldsymbol{s}\| \triangleq 1$. Assuming quasi-static block fading and transmit power P_t (in W), the UL received signal at the n-th RS over subcarrier k is [10]

$$\boldsymbol{y}_{n,k} = \boldsymbol{h}_{n,k} s_k \sqrt{P_\text{t}} + \boldsymbol{w}_{n,k}^{\text{DMC}} s_k + \boldsymbol{z}_{n,k} \quad \in \mathbb{C}^{M\times 1}\ , \quad (1)$$

where $\boldsymbol{w}_{n,k}^{\text{DMC}} \in \mathbb{C}^{M\times 1}$ is due to DMCs and $\boldsymbol{z}_{n,k} \in \mathbb{C}^{M\times 1}$ denotes circularly symmetric complex Gaussian thermal noise with $\boldsymbol{z}_{n,k} \sim \mathcal{CN}_M(\boldsymbol{0}, \frac{\sigma^2}{K}\mathbf{I})$. The total noise power over all K subcarriers is $\sigma^2 = \mathsf{k_B} T B$ where $\mathsf{k_B}$ is the Boltzmann constant, T the absolute temperature, and $B = \Delta_f K$ the bandwidth. $\boldsymbol{h}_{n,k} = \sum_{\ell=0}^{L-1} \boldsymbol{h}_{n,\ell}^{\text{RP}} + \sum_{\iota=1}^{J} \boldsymbol{h}_{n,\iota}^{\text{SP}} \in \mathbb{C}^{M\times 1}$ denotes the multipath channel consisting of a sum of specular multipath components (SMCs) at RPs $\boldsymbol{h}_{n,\ell}^{\text{RP}}$ including the LoS ($\ell = 0$), and reflections at SPs $\boldsymbol{h}_{n,\iota}^{\text{SP}}$. To ease notation, we define the sum channel as

$$\boldsymbol{h}_{n,k} = \sum_{\kappa=0}^{N_\text{c}-1} \rho_{n,\kappa} e^{j\phi_{n,\kappa}} \boldsymbol{a}(\theta_{n,\kappa}) e^{-j2\pi k \Delta_f \widetilde{\tau}_{n,\kappa}}, \quad (2)$$

where $\kappa \in \{0\ \ldots\ N_\text{c}-1\}$ indicates any component out of $N_\text{c} = L + J \triangleq |\mathcal{N}_c|$ (with $\mathcal{N}_c = \mathcal{L} \cup \mathcal{J}$) components impinging on RS n, encompassing the LoS ($\kappa = 0$), all RPs ($\kappa \in \mathcal{L}\backslash\{0\}$), and all SPs ($\kappa \in \mathcal{J}$). The set $\mathcal{L}$ contains the indices of LoS and RPs, and $\mathcal{J} = \{L+1\ \ldots\ L+J\}$ contains SPs, with $L = |\mathcal{L}|$ and $J = |\mathcal{J}|$ being the corresponding set cardinalities. The *unknown* channel parameters for each component κ are: amplitude $\rho_{n,\kappa}$, phase $\phi_{n,\kappa}$, (pseudo-) delay $\widetilde{\tau}_{n,\kappa}$, and AoA $\theta_{n,\kappa}$.

III. Signal and Channel Models

In this section, we first develop a suitable formalization for the channel models of the distributed RSs, emphasizing the fundamental differences between RP and SP channels. Then, our contribution will be to bridge such models to the per-RS observed signal model used to infer the parameters relevant to the localization problem. From the channel parameters in (2),

- the amplitude $\rho_{n,\kappa} \in \mathbb{R}$ represents the magnitude of the forward transmission coefficient[2] between the UE antenna and a hypothetical isotropic antenna at the phase center position $\boldsymbol{p}_n^{\text{RS}}$. Note that we lump together the unknown path amplitude $\rho_{n,\kappa}$ and the known transmit power P_t into a single nuisance parameter $\alpha_{n,\kappa} = \sqrt{P_\text{t}}\rho_{n,\kappa}$, where for notational convenience the LoS amplitude is $\alpha_n^{\text{LoS}} \triangleq \alpha_{n,0}$ (similarly, $\rho_n^{\text{LoS}} \triangleq \rho_{n,0}$).
- $\phi_{n,\kappa}$ is the phase term involving the effects of one-way signal propagation, phase shift induced by reflection, and phase offset between the n^{th} RS and the UE, given by

$$\phi_{n,\kappa} = -2\pi f_\text{c} \tau_{n,\kappa} + \varphi_{n,\kappa} + \delta_{\phi,n}\ , \quad (3)$$

where $\phi_n^{\text{LoS}} \triangleq \phi_{n,0}^{\text{RP}}$ is the LoS component phase and $\tau_{n,\kappa}$ the one-way delay between signal transmission at the UE and reception of component κ at RS n. We use $\tau_n^{\text{LoS}} \triangleq \tau_{n,0}^{\text{RP}}$ to denote the delay of the LoS component. In addition, the reflection-induced phase shift $\varphi_{n,\kappa}$ is assumed unknown for non-line-of-sight (NLoS) components $\kappa > 0$, while $\varphi_{n,0} \triangleq 0$ for the LoS[3].
- $\widetilde{\tau}_{n,\kappa}$ is the pseudo-delay including the effect of one-way propagation and the clock offset of the UE, namely

$$\widetilde{\tau}_{n,\kappa} = \tau_{n,\kappa} + \delta_\tau\ , \quad (4)$$

where the component delay is defined as

$$\tau_{n,\kappa} = \frac{1}{\mathsf{c}} \left(\|\boldsymbol{p} - \boldsymbol{p}_{n,\kappa}^{\text{c}}\| + \|\boldsymbol{p}_{n,\kappa}^{\text{c}} - \boldsymbol{p}_n^{\text{RS}}\| \right) \quad (5)$$

inserting for the position $\boldsymbol{p}_{n,0}^{\text{c}} = \boldsymbol{p}$ for $\kappa = 0$ (LoS), and $\boldsymbol{p}_{n,\kappa}^{\text{c}} = \boldsymbol{p}_{n,\ell}^{\text{RP}}$ for $\kappa \in \mathcal{L}$ or $\boldsymbol{p}_{n,\kappa}^{\text{c}} = \boldsymbol{p}_\iota^{\text{SP}}$ for $\kappa \in \mathcal{J}$ for an RP or SP, respectively. Indices κ are mapped to RP and SP indices using respective functions $\ell(\kappa) = \kappa$ and $\iota(\kappa) = \kappa - L$.
- $\boldsymbol{a}(\theta_{n,\kappa}) \in \mathbb{C}^{M\times 1}$ is the RS array response to a signal impinging with AoA $\theta_{n,\kappa}$ (azimuth relative to the boresight of the n-th RS array). Without loss of generality, we assume that each RS is equipped with a uniform linear array (ULA) with spacing d, so that the array response vector takes the form

$$\boldsymbol{a}(\theta) \triangleq \left[1\ e^{j\frac{2\pi}{\lambda} d \sin\theta}\ \cdots\ e^{j\frac{2\pi}{\lambda} d(M-1)\sin\theta}\right]^\mathsf{T}\ , \quad (6)$$

with $\lambda = \mathsf{c}/f_\text{c}$ denoting the wavelength, and c and f_c denoting the speed of light and carrier frequency, respectively. The AoA $\theta_{n,\kappa}$ relates the known position and orientation of the n-th RS and the unknown UE, RP, or SP position according to

$$\theta_{n,\kappa} = \frac{\pi}{2} - \text{atan2}\left([\boldsymbol{p}'_{n,\kappa}]_2, [\boldsymbol{p}'_{n,\kappa}]_1\right)\ , \quad (7)$$

where $\text{atan2}(y, x)$ denotes the four-quadrant arc tangent function, and we implicitly make the distinction between AoAs of the LoS, RPs, and SPs such that

$$\boldsymbol{p}'_{n,\kappa} = f(\boldsymbol{p}_{n,\kappa}^{\text{c}}) = \boldsymbol{M}^{-1}(\beta_n)(\boldsymbol{p}_{n,\kappa}^{\text{c}} - \boldsymbol{p}_n^{\text{RS}}) \quad (8)$$

is the UE ($\kappa = 0$), RP ($\kappa \in \mathcal{L}\backslash\{0\}$), or SP ($\kappa \in \mathcal{J}$) position in the local reference frame of the n-th RS, and $\boldsymbol{M}(\beta)$ is the rotation matrix around the z-axis (see Supplementary Material S-I) and β_n is the azimuth rotation angle of the RS.

[1]The orientation of each RS is defined by a single angle representing the rotation around the z-axis, meaning that the RSs are parallel to the x-y plane.

[2]The complex channel amplitude $\rho_{n,\kappa} e^{j\phi_{n,\kappa}}$ represents a scattering parameter (S-parameter) such that its squared magnitude corresponds to the path gain between the antenna ports (i.e., the reciprocal of the path loss).

[3]The integer phase ambiguity in $\phi_{n,\kappa}$ in (3) can be entirely absorbed into the unknown phase offset δ_ϕ, thus $\varphi_{n,0} = 0$.

A. Specular Multipath Components

The peculiarity of a specular reflection at a surface is that the incident and reflected rays form equal angles with the surface normal. Such specular reflections typically occur when the wavelength is large compared to the surface roughness [40]. Specular reflections at large planar surfaces are particularly relevant indoors, which we model through a geometric channel [41]. The point at a specularly reflecting surface where a ray cast by the UE impinges before getting reflected to the n-th RS is denoted $\boldsymbol{p}^{\text{RP}}_{n,\ell}$ and defined through our geometric model in Supplementary Material S-II-A. With $\theta^{\text{LoS}}_n \triangleq \theta_{n,0}$ denoting the AoA of the LoS component, the AoAs of RPs $\theta^{\text{RP}}_{n,\ell}$ are described through (7) by inserting the RP position $\boldsymbol{p}^{\text{RP}}_{n,\ell}$ (8). While the LoS delay $\tau^{\text{LoS}}_n = \frac{1}{\mathsf{c}}\|\boldsymbol{p}-\boldsymbol{p}^{\text{RS}}_n\|$, the RP delay $\tau^{\text{RP}}_{n,\ell}$ is computed by inserting $\boldsymbol{p}^{\text{RP}}_{n,\ell}$ in (5), which describes the propagation from the UE over the ℓ-th RP of RS n to its phase center position. This will be referred to as *RP channel model*, where we relate the amplitudes $\alpha^{\text{RP}}_{n,\ell}$ and phases $\phi^{\text{RP}}_{n,\ell}$ to the environment geometry through the Friis equation reformulated for power-wave amplitudes, defined in Supplementary Material S-II-B. We consider L specular surfaces, each of which would give rise to a single RP per RS n. However, each RS is mounted on a surface that does not produce an SMC for that respective RS, thus the total number of RPs including the LoS equals L for each RS.

B. Scatter Point Components

Contrary to the unidirectional scattering (i.e., equal incident and reflecting angles) of a specular reflection at a large planar surface, the characteristic feature of a reflection at an SP is its omnidirectional rescattering. In real-life scenarios, small metallic objects, corners, metal poles, or window frames often possess the characteristics of SPs [42]. An SP component originates from the UE position, impinges at the ι-th SP at $\boldsymbol{p}^{\text{SP}}_{\iota}$ and travels to the n-th RS at $\boldsymbol{p}^{\text{RS}}_n$. The AoAs of SPs $\theta^{\text{SP}}_{n,\iota}$ are described through (7) by inserting the SP position $\boldsymbol{p}^{\text{SP}}_{\iota}$ in (8). The SP component delay is computed by inserting $\boldsymbol{p}^{\text{SP}}_{\iota}$ in (5). This will be referred to as *SP channel model*, where we relate the amplitudes $\alpha^{\text{SP}}_{n,\iota}$ and phases $\phi^{\text{SP}}_{n,\iota}$ to the environment geometry through the bistatic radar range equation reformulated for power-wave amplitudes, defined in Supplementary Material S-II-C.

C. Dense Multipath Components

The dense multipath term in (1) can be modeled as a stochastic component with the distribution [10], [36], [43]

$$\boldsymbol{w}^{\text{DMC}}_n \sim \mathcal{CN}_{MK}(\boldsymbol{0}, \boldsymbol{R}^{\text{DMC}}(\boldsymbol{\eta}_{\text{DMC}})) \ , \tag{9}$$

where

$$\boldsymbol{w}^{\text{DMC}}_n \triangleq [(\boldsymbol{w}^{\text{DMC}}_{n,0})^{\mathsf{T}} \ \cdots \ (\boldsymbol{w}^{\text{DMC}}_{n,K-1})^{\mathsf{T}}]^{\mathsf{T}} \quad \in \mathbb{C}^{MK\times 1} \tag{10}$$

denotes the DMC observed in the spatial-frequency domain, and $\boldsymbol{R}^{\text{DMC}} \in \mathbb{C}^{MK\times MK}$ is the spatial-frequency covariance matrix of the DMC. Assuming spatially white DMC and the Kronecker separability of the spatial and frequency domains (i.e., uncorrelated scattering between angle and delay domains), $\boldsymbol{R}^{\text{DMC}}$ can be written as [34, Eq. (2.69)], [10], [43]

$$\boldsymbol{R}^{\text{DMC}}(\boldsymbol{\eta}_{\text{DMC}}) = \boldsymbol{R}_f(\boldsymbol{\eta}_{\text{DMC}}) \otimes \mathbf{I}_M \ , \tag{11}$$

where $\boldsymbol{R}_f(\boldsymbol{\eta}_{\text{DMC}}) = \text{Toep}(\boldsymbol{\kappa}(\boldsymbol{\eta}_{\text{DMC}}), \boldsymbol{\kappa}(\boldsymbol{\eta}_{\text{DMC}})^{\mathsf{H}}) \in \mathbb{C}^{K\times K}$ is the frequency domain covariance matrix where $\boldsymbol{\eta}_{\text{DMC}} = [\alpha_{\text{d}} \ \beta_{\text{d}} \ \tau_{\text{d}}]^{\mathsf{T}}$ is the DMC parameter vector consisting of power α_{d}, normalized coherence bandwidth β_{d}, and normalized onset time τ_{d}, and $\boldsymbol{\kappa}(\boldsymbol{\eta}_{\text{DMC}}) \in \mathbb{C}^{K\times 1}$ represents the sampled version of the DMC power spectral density [34, Eq. (2.61)]

$$\psi_{\text{DMC}}(f) = \frac{\alpha_{\text{d}}}{\beta_{\text{d}} + j2\pi f} \ e^{-j2\pi f\tau_{\text{d}}} \ . \tag{12}$$

D. Spatial-Frequency Observations at Radio Stripes

Aggregating the received signals in (1) over K subcarriers, using the multipath model in (2) and DMC model in (9), the spatial-frequency observation matrix at the n-th RS is

$$\begin{aligned}\boldsymbol{Y}_n &\triangleq [\boldsymbol{y}_{n,0} \ \cdots \ \boldsymbol{y}_{n,K-1}] \quad \in \mathbb{C}^{M\times K} \\ &= \sum_{\kappa=0}^{N_{\text{c}}-1} \alpha_{n,\kappa} e^{j\phi_{n,\kappa}} \boldsymbol{a}(\theta_{n,\kappa})(\boldsymbol{b}(\widetilde{\tau}_{n,\kappa}) \odot \boldsymbol{s})^{\mathsf{T}} + \boldsymbol{W}_n \ ,\end{aligned} \tag{13}$$

where

$$\boldsymbol{b}(\tau) \triangleq \left[1 \ e^{-j2\pi\Delta_f\tau} \ \cdots \ e^{-j2\pi(K-1)\Delta_f\tau}\right]^{\mathsf{T}} \in \mathbb{C}^{K\times 1} \tag{14}$$

is the frequency domain steering vector, and

$$\boldsymbol{W}_n = \boldsymbol{W}^{\text{DMC}}_n \odot \left(\mathbf{1}_{M\times 1}\boldsymbol{s}^{\mathsf{T}}\right) + \boldsymbol{Z}_n \quad \in \mathbb{C}^{M\times K} \tag{15}$$

is the disturbance term consisting of DMCs and white noise, with $\boldsymbol{W}^{\text{DMC}}_n = \text{reshape}_{M,K}(\boldsymbol{w}^{\text{DMC}}_n) \in \mathbb{C}^{M\times K}$ and $\boldsymbol{Z}_n = [\boldsymbol{z}_{n,0} \ \cdots \boldsymbol{z}_{n,K-1}] \in \mathbb{C}^{M\times K}$. From Supplementary Material S-III, we have[4]

$$\boldsymbol{w}_n = \text{vec}\,(\boldsymbol{W}_n) \sim \mathcal{CN}_{MK}(\boldsymbol{0}, \boldsymbol{R}(\boldsymbol{\eta}_{\text{DMC}}, \sigma^2)) \ , \tag{16}$$

where

$$\boldsymbol{R}(\boldsymbol{\eta}_{\text{DMC}}, \sigma^2) = \left(\boldsymbol{R}_f(\boldsymbol{\eta}_{\text{DMC}}) \odot \boldsymbol{s}\boldsymbol{s}^{\mathsf{H}}\right) \otimes \mathbf{I}_M + \frac{\sigma^2}{K}\mathbf{I}_{MK} \ . \tag{17}$$

E. SDNR Definition

For comparability of results in Sec. VII-A, we relate the signal-to-dense multipath-plus-noise ratio (SDNR) only to the LoS and define the average SDNR as[5]

$$\text{SDNR} = \frac{P_{\text{t}}}{NK}\sum_{n=1}^{N}(\rho^{\text{LoS}}_n)^2 \ \|\boldsymbol{c}'(\theta^{\text{LoS}}_n, \widetilde{\tau}^{\text{LoS}}_n)\|^2 \, , \tag{18}$$

where the per-RS angular-delay response is $\boldsymbol{c}(\theta,\tau) \triangleq (\boldsymbol{b}(\tau) \odot \boldsymbol{s}) \otimes \boldsymbol{a}(\theta) \in \mathbb{C}^{MK\times 1}$ and $\boldsymbol{c}'(\theta,\tau) \triangleq \boldsymbol{R}^{-1/2}\boldsymbol{c}(\theta,\tau)$. The ratio of DMC power to thermal noise power is defined through the dense-multipath-to-noise ratio (DNR) $\text{DNR} = \frac{\alpha_{\text{d}}}{\sigma^2}$. For simulations, we keep the SDNR in (18) constant and set the transmit power

$$P_{\text{t}} = \frac{\text{SDNR} \ NK}{\sum_{n=1}^{N}(\rho^{\text{LoS}}_n)^2 \ \|\boldsymbol{c}'(\theta^{\text{LoS}}_n, \widetilde{\tau}^{\text{LoS}}_n)\|^2} \tag{19}$$

to meet the desired SDNR for the chosen parameters.

[4]The DMC statistics may not be the same among the RSs since the distances between each RS and the UE are different. This leads to different power, coherence bandwidth, and onset time for each RS. See [10].

[5]M does not enter in the denominator of (18). This effectively divides (19) by M and ensures that the positioning accuracy depends only on the *angular resolution* and not the *array gain* (cf. Fig. 4(a) and Fig. 4(b)).

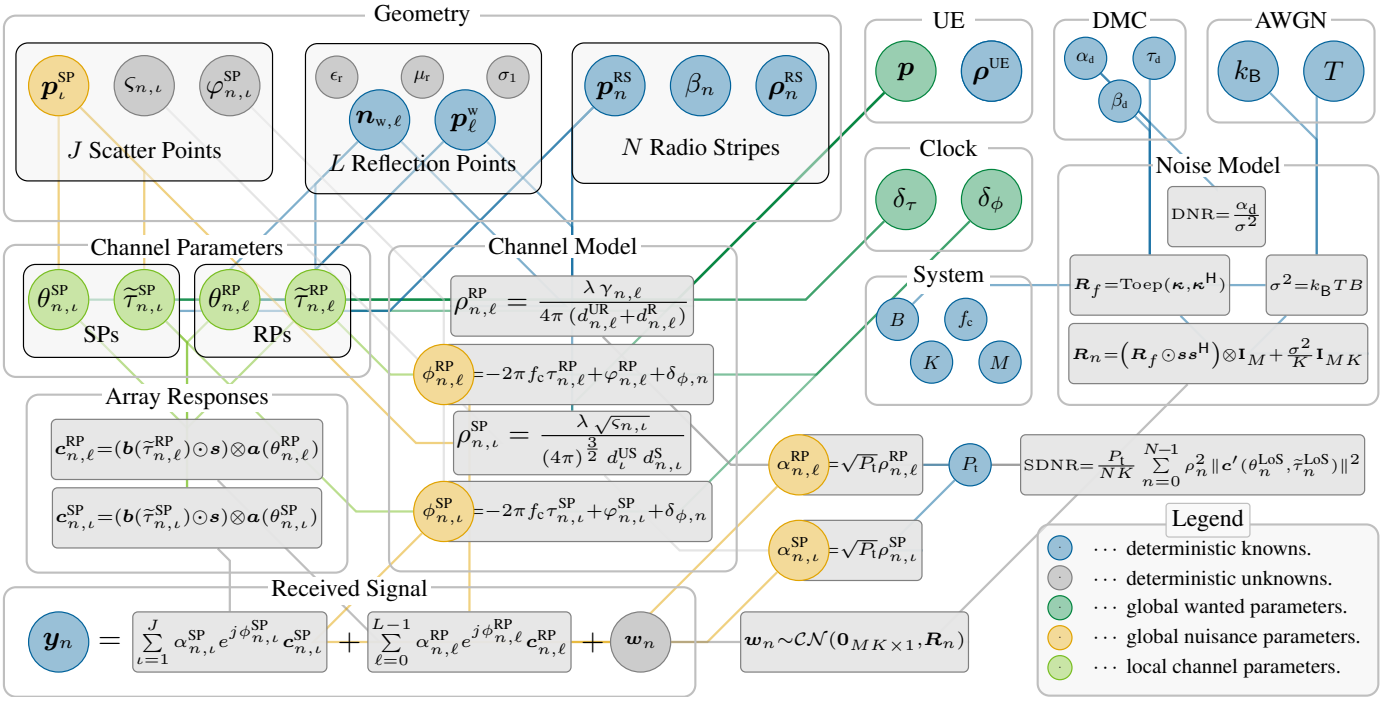

Fig. 2. A non-exhaustive overview of our signal model defined in Sec. III with parameters indicated by nodes and dependencies represented by edges. We distinguish global parameters of interest $\boldsymbol{\eta}_\mathrm{w}$ and global nuisance parameters $\boldsymbol{\eta}_\mathrm{u}$ from (20), and local per-RS channel parameters $\boldsymbol{\eta}_n^\mathrm{ch}$ from (66).

IV. Problem Formulation

The joint positioning, synchronization and mapping problem consists in inferring a set of wanted parameters from signal observations at each RS either using intermediate channel parameters (*two-step*) or by *direct* fusion of the acquired information at the RSs network level. Given the observations $\{\boldsymbol{Y}_n\}_{n=0}^{N-1}$ in (13) collected by all RSs from only a *single snapshot* of UL transmission, the problem of interest is to estimate the UE position $\boldsymbol{p}$, its clock offset δ_τ and its phase offsets $\delta_{\phi,n}$, and the SP positions $\boldsymbol{p}_\iota^\mathrm{SP}$, contrary to RP positions.[6] As to DMC parameters, different methods are available to estimate them, e.g. [10, Sec. III-C1], [34, Sec. 6.1.8]. To decouple the less investigated problem of joint localization, synchronization, and mapping supported by a network of distributed RSs from the better-understood problem of estimating DMC parameters, we assume that preliminary estimation of $\boldsymbol{R}^\mathrm{DMC}(\boldsymbol{\eta}_\mathrm{DMC})$ has been performed by resorting to one of those methods. The unknown parameter vector for our estimation problem is then defined as

$$\boldsymbol{\eta} = \big[\underbrace{\boldsymbol{p}^\mathsf{T}\ \boldsymbol{\delta}^\mathsf{T}\ \boldsymbol{p}^{\mathrm{SP}\mathsf{T}}}_{\boldsymbol{\eta}_\mathrm{w}}\ \underbrace{\boldsymbol{\phi}^\mathsf{T}\ \boldsymbol{\alpha}^\mathsf{T}}_{\boldsymbol{\eta}_\mathrm{u}}\big]^\mathsf{T} \in \mathbb{R}^{\mathcal{D}_\mathrm{g}\times 1}, \tag{20}$$

which is divided into parameters of interest $\boldsymbol{\eta}_\mathrm{w}$ and nuisance parameters $\boldsymbol{\eta}_\mathrm{u}$, and where

$$\boldsymbol{\delta} := [\delta_\tau\ \boldsymbol{\delta}_\phi^\mathsf{T}]^\mathsf{T}, \tag{21a}$$
$$\boldsymbol{p}^\mathrm{SP} := [\boldsymbol{p}_1^{\mathrm{SP}\mathsf{T}}\ \dots\ \boldsymbol{p}_J^{\mathrm{SP}\mathsf{T}}]^\mathsf{T} \in \mathbb{R}^{3J\times 1}, \tag{21b}$$
$$\boldsymbol{\alpha}_n := [\alpha_{n,0}\ \dots\ \alpha_{n,N_\mathrm{c}-1}]^\mathsf{T} \in \mathbb{R}^{N_\mathrm{c}\times 1}, \tag{21c}$$
$$\boldsymbol{\alpha} := [\boldsymbol{\alpha}_1^\mathsf{T}\ \dots\ \boldsymbol{\alpha}_N^\mathsf{T}]^\mathsf{T} \in \mathbb{R}^{NN_\mathrm{c}\times 1}, \tag{21d}$$
$$\boldsymbol{\phi}_n := [\phi_{n,1}\ \dots\ \phi_{n,N_\mathrm{c}-1}]^\mathsf{T} \in \mathbb{R}^{N_\mathrm{c}-1\times 1}, \tag{21e}$$
$$\boldsymbol{\phi} := [\boldsymbol{\phi}_1^\mathsf{T}\ \dots\ \boldsymbol{\phi}_{N_\mathrm{c}-1}^\mathsf{T}]^\mathsf{T} \in \mathbb{R}^{N(N_\mathrm{c}-1)\times 1}. \tag{21f}$$

[6] Since walls have known positions and orientations, $\boldsymbol{p}_{n,\ell}^\mathrm{RP}$ can be expressed through the UE position $\boldsymbol{p}$ (contained in $\boldsymbol{\eta}$) according to our model in Supplementary Material S-II-A and do not enter $\boldsymbol{\eta}$ as nuisance parameters.

Parameters of interest: We aim to infer the UE position $\boldsymbol{p}$ and synchronization parameters, $\boldsymbol{\delta} := [\delta_\tau, \boldsymbol{\delta}_\phi^\mathsf{T}]^\mathsf{T}$ where we distinguish two different levels of phase synchronization:

- NCP *Noncoherent* processing: $\boldsymbol{\delta}$ encompasses a time offset δ_τ and a phase offset $\delta_{\phi,n}$ to each RS $\boldsymbol{\delta}_\phi = [\delta_{\phi,1}\cdots\delta_{\phi,N}]^\mathsf{T}$, thus $\boldsymbol{\delta} \in \mathbb{R}^{1+N\times 1}$.
- CP *Coherent* processing: $\boldsymbol{\delta}$ encompasses a time offset δ_τ and one phase offset δ_ϕ to all RSs, i.e., $\boldsymbol{\delta} = [\delta_\tau\ \delta_\phi]^\mathsf{T} \in \mathbb{R}^{2\times 1}$.

Depending on the level of synchronization, the dimension of the global parameter vector $\boldsymbol{\eta}$ is

$$\mathcal{D}_\mathrm{g} = \begin{cases} D+1+3J+2N(L+J) & \text{NCP} \\ D+2+3J+2N(L+J)-N & \text{CP} \end{cases}, \tag{22}$$

where D indicates the number of unknown UE position coordinates.[7] In addition, we want to map the environment in terms of dominant obstacles and use $\boldsymbol{p}^\mathrm{SP} \in \mathbb{R}^{3J\times 1}$ to denote the vector of stacked SP positions $\boldsymbol{p}_\iota^\mathrm{SP} \in \mathbb{R}^{3\times 1}$.

Nuisance parameters: While $\boldsymbol{\alpha}_n$ contains the N_c stacked amplitudes of all components impinging at a single RS n, we stack the amplitudes of the total number of NN_c components impinging on all N RSs into a vector $\boldsymbol{\alpha}$. Likewise, we stack all phases except for the LoS $\kappa = 0$ in a vector $\boldsymbol{\phi}_n$ and stack the phases of the total number of RPs and SPs impinging on all RSs into a vector $\boldsymbol{\phi}$. The phases ϕ_n^LoS of LoS components are not entering our nuisance parameters $\boldsymbol{\eta}_\mathrm{u}$, as they are implicitly contained in the remaining parameters of our global parameter vector $\boldsymbol{\eta}$, according to our channel model defined in Sec. III-A.

[7] Setting $D = 2$ requires one coordinate of the UE antenna to be known, e.g., positioning a robot with fixed and known antenna height (sometimes termed 2.5D positioning).

V. Joint Positioning, Synchronization and Mapping in Radio Stripes Networks

We derive novel reduced-complexity algorithms to solve the joint positioning, synchronization and mapping problem in Sec. IV. We consider phase-coherent RSs (CP), namely $\boldsymbol{\delta} = [\delta_\tau \ \delta_\phi]^\mathsf{T}$, which unveils the potential of the RS network: the spatial distribution of the RSs provides a large aperture, enabling exploitation of spherical wavefront information under near-field conditions, bringing in turn high-resolution carrier phase information to estimate UE/SP positions.

A. Optimal Joint Localization, Synchronization and Mapping via Maximum Likelihood

Following the Maximum Likelihood (ML) approach, we frame the positioning, synchronization, and mapping problem as a *direct* joint estimation problem, hereafter referred to as Joint ML (JML):

$$\widehat{\boldsymbol{\eta}}^{\text{JML}} = \arg\max_{\boldsymbol{\eta}} \ p(\{\boldsymbol{Y}_n\}_{n=1}^N \mid \boldsymbol{\eta}), \tag{23}$$

with $p(\{\boldsymbol{Y}_n\}_{n=1}^N \mid \boldsymbol{\eta})$ the joint probability density function (PDF) of all observables conditioned on $\boldsymbol{\eta}$, of which the vector of desired parameters is $\boldsymbol{\eta}_{\text{w}} = [\boldsymbol{p}^\mathsf{T} \ \delta_\tau \ \delta_\phi \ \boldsymbol{p}^{\text{SP}\mathsf{T}}]^\mathsf{T}$ in the CP case.

Assuming independent realizations of the disturbance component $\boldsymbol{W}_n$ in (15) across the RSs, the log-likelihood version of the objective in (23) can be written as

$$\log p(\{\boldsymbol{Y}_n\}_{n=1}^N \mid \boldsymbol{\eta}) = \sum_{n=1}^N \log p(\boldsymbol{Y}_n \mid \boldsymbol{\eta}) \ , \tag{24}$$

where

$$\log \ p(\boldsymbol{Y}_n \mid \boldsymbol{\eta}) = -\Big\| \boldsymbol{R}_n^{-1/2} \Big[\boldsymbol{y}_n - \sum_{\ell=0}^{L-1} \gamma_{n,\ell}^{\text{RP}} \, \boldsymbol{c}(\theta_{n,\ell}^{\text{RP}}, \widetilde{\tau}_{n,\ell}^{\text{RP}}) - \sum_{\iota=1}^{J} \gamma_{n,\iota}^{\text{SP}} \, \boldsymbol{c}(\theta_{n,\iota}^{\text{SP}}, \widetilde{\tau}_{n,\iota}^{\text{SP}}) \Big] \Big\|^2 - MK \log \pi - \log\det \boldsymbol{R}_n \ , \tag{25}$$

with $\gamma_{n,\ell}^{\text{RP}} = \alpha_{n,\ell}^{\text{RP}} e^{j\phi_{n,\ell}^{\text{RP}}}$, $\gamma_{n,\iota}^{\text{SP}} = \alpha_{n,\iota}^{\text{SP}} e^{j\phi_{n,\iota}^{\text{SP}}}$, L includes the LoS path and the known number of RPs, $\boldsymbol{R}_n$ is defined in (17), and $\boldsymbol{y}_n \triangleq \text{vec}\,(\boldsymbol{Y}_n) \in \mathbb{C}^{MK\times 1}$ is the vectorized form of the data matrix $\boldsymbol{Y}_n$ (13) at n-th RS. Notice that, while coarse knowledge of the number of RPs ($L-1$) is generally available (being dependent on the number of walls, ceiling and other large reflecting surfaces, easily obtained from the building structural layout), knowledge of J can be more challenging due to the less predictable nature of scattering. However, also this value can be estimated from the observations using classical techniques for model order selection, e.g. Akaike's method [44]), hence in the following J is assumed known.

Neglecting constant terms in (25), problem (23) becomes

$$\widehat{\boldsymbol{\eta}}^{\text{JML}} = \arg\min_{\boldsymbol{\eta}} \ \mathcal{L}^{\text{JML}}(\boldsymbol{\eta}) \ , \tag{26}$$

where we pose $\boldsymbol{y}'_n \triangleq \boldsymbol{R}_n^{-1/2}\boldsymbol{y}_n$ and

$$\mathcal{L}^{\text{JML}}(\boldsymbol{\eta}) = \sum_{n=1}^N \Big\| \boldsymbol{y}'_n - \sum_{\ell=0}^{L-1} \gamma_{n,\ell}^{\text{RP}} \, \boldsymbol{c}'(\theta_{n,\ell}^{\text{RP}}, \widetilde{\tau}_{n,\ell}^{\text{RP}}) - \sum_{\iota=1}^{J} \gamma_{n,\iota}^{\text{SP}} \, \boldsymbol{c}'(\theta_{n,\iota}^{\text{SP}}, \widetilde{\tau}_{n,\iota}^{\text{SP}}) \Big\|^2 . \tag{27}$$

To tackle the challenging optimization problem above, we re-parameterize (27) in a different but equivalent form as

$$\mathcal{L}^{\text{JML}}(\boldsymbol{\eta}) = \sum_{n=1}^N \Big\| \boldsymbol{y}'_n - \boldsymbol{B}_n(\boldsymbol{\eta}_{\text{w}}) \boldsymbol{x}_n(\boldsymbol{\alpha}_n, \boldsymbol{\phi}_n) \Big\|^2 , \tag{28}$$

where $\boldsymbol{x}_n$ is a $(2(L+J)-1)\times 1$ *real* vector stacking the real amplitude α_n^{LoS} of the LOS path and both the real and imaginary parts of each complex RPs and SPs amplitudes, i.e.,

$$\boldsymbol{x}_n = [\alpha_n^{\text{LoS}}, \Re\{\gamma_{n,1}^{\text{RP}}\}, \Im\{\gamma_{n,1}^{\text{RP}}\}, \cdots, \Re\{\gamma_{n,L-1}^{\text{RP}}\}, \Im\{\gamma_{n,L-1}^{\text{RP}}\}, \Re\{\gamma_{n,1}^{\text{SP}}\}, \Im\{\gamma_{n,1}^{\text{SP}}\}, \cdots, \Re\{\gamma_{n,J}^{\text{SP}}\}, \Im\{\gamma_{n,J}^{\text{SP}}\}]^\mathsf{T}, \tag{29}$$

with $\boldsymbol{B}_n \in \mathbb{C}^{MK\times(2(L+J)-1)}$ given by

$$\boldsymbol{B}_n = [e^{j\phi_n^{\text{LoS}}} \boldsymbol{c}'(\theta_n^{\text{LoS}}, \widetilde{\tau}_n^{\text{LoS}}), \boldsymbol{c}'(\theta_{n,1}^{\text{RP}}, \widetilde{\tau}_{n,1}^{\text{RP}}), j\boldsymbol{c}'(\theta_{n,1}^{\text{RP}}, \widetilde{\tau}_{n,1}^{\text{RP}}), \cdots \boldsymbol{c}'(\theta_{n,L-1}^{\text{RP}}, \widetilde{\tau}_{n,L-1}^{\text{RP}}), j\boldsymbol{c}'(\theta_{n,L-1}^{\text{RP}}, \widetilde{\tau}_{n,L-1}^{\text{RP}}), \boldsymbol{c}'(\theta_{n,1}^{\text{SP}}, \widetilde{\tau}_{n,1}^{\text{SP}}), j\boldsymbol{c}'(\theta_{n,1}^{\text{SP}}, \widetilde{\tau}_{n,1}^{\text{SP}}), \cdots, \boldsymbol{c}'(\theta_{n,J}^{\text{SP}}, \widetilde{\tau}_{n,J}^{\text{SP}}), j\boldsymbol{c}'(\theta_{n,J}^{\text{SP}}, \widetilde{\tau}_{n,J}^{\text{SP}})]. \tag{30}$$

Then, we notice that

$$\begin{aligned} \Big\| \boldsymbol{y}'_n - \boldsymbol{B}_n\boldsymbol{x}_n \Big\|^2 &= \Big\| (\boldsymbol{y}'_{n,R} + j\boldsymbol{y}'_{n,I}) - (\boldsymbol{B}_{n,R} + j\boldsymbol{B}_{n,I})\boldsymbol{x}_n \Big\|^2 \\ &= \Big\| \boldsymbol{y}'_{n,R} - \boldsymbol{B}_{n,R}\boldsymbol{x}_n + j(\boldsymbol{y}'_{n,I} - \boldsymbol{B}_{n,I}\boldsymbol{x}_n) \Big\|^2 \\ &= \Big\| \boldsymbol{y}'_{n,R} - \boldsymbol{B}_{n,R}\boldsymbol{x}_n \Big\|^2 + \Big\| \boldsymbol{y}'_{n,I} - \boldsymbol{B}_{n,I}\boldsymbol{x}_n \Big\|^2 , \end{aligned} \tag{31}$$

where $\boldsymbol{y}'_{n,R} = \Re\{\boldsymbol{y}'_n\}$, $\boldsymbol{y}'_{n,I} = \Im\{\boldsymbol{y}'_n\}$ and, similarly, $\boldsymbol{B}_{n,R} = \Re\{\boldsymbol{B}_n\}$, $\boldsymbol{B}_{n,I} = \Im\{\boldsymbol{B}_n\}$. The expression in (31) is a convenient decomposition that allows us to obtain the optimal (ML) estimates of $\boldsymbol{x}_n$'s in closed-form. More specifically, by computing the derivative of $\mathcal{L}(\boldsymbol{\eta})$ in (28) using (31) wrt each vector $\boldsymbol{x}_n$, $n = 1, \ldots, N$, and posing it equal to zero, it follows

$$(\boldsymbol{B}_{n,R}^\mathsf{T}\boldsymbol{B}_{n,R} + \boldsymbol{B}_{n,I}^\mathsf{T}\boldsymbol{B}_{n,I})\boldsymbol{x}_n = \boldsymbol{B}_{n,R}^\mathsf{T}\boldsymbol{y}'_{n,R} + \boldsymbol{B}_{n,I}^\mathsf{T}\boldsymbol{y}'_{n,I} \tag{32}$$

since the $\boldsymbol{x}_n$'s are not linked to each other and, accordingly, terms in the outer summation of $\mathcal{L}(\boldsymbol{\eta})$ corresponding to RSs with indexes $n' \neq n$ will be constant when derived wrt $\boldsymbol{x}_n$. Re-arranging the terms in

$$\mathring{\boldsymbol{y}}'_n = \begin{bmatrix} \boldsymbol{y}'_{n,R} \\ \boldsymbol{y}'_{n,I} \end{bmatrix}, \qquad \mathring{\boldsymbol{B}}_n = \begin{bmatrix} \boldsymbol{B}_{n,R} \\ \boldsymbol{B}_{n,I} \end{bmatrix} \tag{33}$$

we can finally obtain a closed-form estimate of the corresponding $\boldsymbol{x}_n$ in terms of $\boldsymbol{B}_n$ for each individual RS n as

$$(\mathring{\boldsymbol{B}}_n^\mathsf{T}\mathring{\boldsymbol{B}}_n)\boldsymbol{x}_n = \mathring{\boldsymbol{B}}_n^\mathsf{T}\mathring{\boldsymbol{y}}'_n \quad \longrightarrow \quad \widehat{\boldsymbol{x}}_n^{\text{JML}} = \mathring{\boldsymbol{B}}_n^\dagger\mathring{\boldsymbol{y}}'_n, \tag{34}$$

with $\mathring{\boldsymbol{B}}_n^\dagger = \left(\mathring{\boldsymbol{B}}_n^\mathsf{T}\mathring{\boldsymbol{B}}_n\right)^{-1}\mathring{\boldsymbol{B}}_n^\mathsf{T}$. From (34), one can easily retrieve the estimates of the real LoS amplitudes α_n^{LoS}'s as well as the complex multipath amplitudes $\gamma_{n,\ell}^{\text{RP}}$'s and $\gamma_{n,\iota}^{\text{SP}}$'s as

$$\widehat{\alpha}_n^{\text{LoS, JML}} = [\widehat{\boldsymbol{x}}_n^{\text{JML}}]_1 \tag{35}$$

$$\widehat{\gamma}_{n,\ell}^{\text{RP, JML}} = [\widehat{\boldsymbol{x}}_n^{\text{JML}}]_{2\ell} + j[\widehat{\boldsymbol{x}}_n^{\text{JML}}]_{2\ell+1}, \ \ell = 1, \ldots, L-1 \tag{36}$$

$$\widehat{\gamma}_{n,\iota}^{\text{SP, JML}} = [\widehat{\boldsymbol{x}}_n^{\text{JML}}]_{2(L-1)+2\iota} + j[\widehat{\boldsymbol{x}}_n^{\text{JML}}]_{2L+2\iota-1}, \ \iota = 1, \ldots, J, \tag{37}$$

with $[\cdot]_i$ indicating the i-th element of the vector argument.

Now that we have obtained optimal estimates $\widehat{\boldsymbol{x}}_n^{\text{JML}}$ of the path amplitudes in (34), which correspond to the $\boldsymbol{\eta}_{\text{u}}$ part of $\boldsymbol{\eta}$ in (20), we can plug $\widehat{\boldsymbol{x}}_n^{\text{JML}}$, $n = 1, \ldots, N$, back into (28) to obtain the following compressed log-likelihood function

$$\mathcal{L}^{\text{JML}}(\boldsymbol{\eta}_{\text{w}}) = \sum_{n=1}^N \Big\| \boldsymbol{y}'_n - \boldsymbol{B}_n(\boldsymbol{\eta}_{\text{w}})\mathring{\boldsymbol{B}}_n^\dagger(\boldsymbol{\eta}_{\text{w}})\mathring{\boldsymbol{y}}'_n \Big\|^2 . \tag{38}$$

Remarkably, the dimension of the estimation problem has been reduced from $D + 2 + 3J + N(2L + 2J - 1)$ to $D + 2 + 3J$. By inspecting (38) and using (30), it is possible to highlight the dependence of $\boldsymbol{B}_n$ (similarly of $\mathring{\boldsymbol{B}}_n^\dagger$) on the remaining

unknown parameters, namely UE position $\boldsymbol{p}$, clock offset δ_τ, phase offset δ_ϕ, and SP positions $\{\boldsymbol{p}_\iota^{\text{SP}}\}_{\iota=1}^J$, as follows:

- ϕ_n^{LoS} depends on $\boldsymbol{p}$ and δ_ϕ through (3) and (5);
- $\widetilde{\tau}_{n,\ell}^{\text{RP}}$ can be written in terms of $\boldsymbol{p}$, $\boldsymbol{p}_{n,\ell}^{\text{RP}}$ and δ_τ through (5) and (4), and in turn $\boldsymbol{p}_{n,\ell}^{\text{RP}}$ can be written as a function of $\boldsymbol{p}$ via (S2) (see Supplementary Material S-II-A);
- $\theta_{n,\ell}^{\text{RP}}$ can be written in terms of $\boldsymbol{p}$ and $\boldsymbol{p}_{n,\ell}^{\text{RP}}$ through (7)-(8);
- $\widetilde{\tau}_{n,\iota}^{\text{SP}}$ depends on $\boldsymbol{p}$, $\boldsymbol{p}_\iota^{\text{SP}}$ and δ_τ through (4) and (5);
- $\theta_{n,\iota}^{\text{SP}}$ depends on $\boldsymbol{p}$ and $\boldsymbol{p}_\iota^{\text{SP}}$ through (7) and (8).

Interestingly, the dependencies left are only upon the parameters of interest $\boldsymbol{\eta}_{\text{w}} = [\boldsymbol{p}^{\mathsf{T}}\ \delta_\tau\ \delta_\phi\ \boldsymbol{p}^{\text{SP}\mathsf{T}}]^{\mathsf{T}}$. In principle, solving the estimation problem

$$\widehat{\boldsymbol{\eta}}_{\text{w}}^{\text{JML}} = \arg\min_{\boldsymbol{\eta}_{\text{w}}}\ \mathcal{L}^{\text{JML}}(\boldsymbol{\eta}_{\text{w}}) \tag{39}$$

would require a joint optimization over the continuous support defined by $\boldsymbol{\eta}_{\text{w}}$, which unfortunately is not feasible in closed-form, nor can be approached by an exhaustive grid search due to the exceptionally high dimensionality of the problem. Therefore, in the following we propose a novel approach to make the estimation task feasible. Specifically, we derive novel approximate estimators that can provide good initial estimates of the parameters in $\boldsymbol{\eta}_{\text{w}}$; then, the latter will be used to initialize an iterative, reduced-complexity optimization of the optimal compressed log-likelihood function in (38), ultimately yielding refined estimates that we retain.

B. Reduced-complexity Algorithms for Initial UE Localization, Synchronization and Mapping

To tackle the formidable complexity of the problem at hand, we follow an alternative strategy, hereafter referred to as *Relaxed Maximum Likelihood (RML)*. The main idea consists in decoupling the estimation of the UE-related parameters $\breve{\boldsymbol{\eta}}_{\text{w}} = [\boldsymbol{p}^{\mathsf{T}}\ \delta_\tau\ \delta_\phi]^{\mathsf{T}}$ from the SP parameters $\{\boldsymbol{p}_\iota^{\text{SP}}\}_{\iota=1}^J$, and relaxing some dependencies, as discussed in the following.

1) Initial UE Localization and Synchronization: We start by relaxing the original estimation problem in (39) and propose to approximate the signal model as consisting of LoS and RPs contributions only, which is tantamount to neglecting, at a first stage, the presence of the J paths originating from SPs $\{\boldsymbol{p}_\iota^{\text{SP}}\}_{\iota=1}^{J-1}$. Accordingly, (27) becomes

$$\mathcal{L}^{\text{RML}}(\breve{\boldsymbol{\eta}}) = \sum_{n=1}^{N} \Big\| \boldsymbol{y}'_n - \alpha_n^{\text{LoS}} e^{j\phi_n^{\text{LoS}}} \boldsymbol{c}'(\theta_n^{\text{LoS}}, \widetilde{\tau}_n^{\text{LoS}}) - \sum_{\ell=1}^{L-1} \gamma_{n,\ell}^{\text{RP}}\, \boldsymbol{c}'(\theta_{n,\ell}^{\text{RP}}, \widetilde{\tau}_{n,\ell}^{\text{RP}}) \Big\|^2, \tag{40}$$

with $\breve{\boldsymbol{\eta}} = [\underbrace{\boldsymbol{p}^{\mathsf{T}}\ \delta_\tau\ \delta_\phi}_{\breve{\boldsymbol{\eta}}_{\text{w}}}\ \underbrace{\boldsymbol{\alpha}^{\text{RP}}\ \boldsymbol{\phi}^{\text{RP}}}_{\breve{\boldsymbol{\eta}}_{\text{u}}}]^{\mathsf{T}} \in \mathbb{R}^{(D+2+N(2L-1))\times 1}$ and

$$\boldsymbol{\alpha}^{\text{RP}} \triangleq [\boldsymbol{\alpha}_1^{\text{RP}\mathsf{T}}\ \cdots\ \boldsymbol{\alpha}_N^{\text{RP}\mathsf{T}}]^{\mathsf{T}} \in \mathbb{R}^{NL\times 1}\ , \tag{41a}$$

$$\boldsymbol{\phi}^{\text{RP}} \triangleq [[\boldsymbol{\phi}_1^{\text{RP}}]_{2:L}^{\mathsf{T}}\ \cdots\ [\boldsymbol{\phi}_N^{\text{RP}}]_{2:L}^{\mathsf{T}}]^{\mathsf{T}} \in \mathbb{R}^{N(L-1)\times 1}\ . \tag{41b}$$

a) Estimation of Phase Offset: We now provide a strategy to obtain a closed-form estimate of the phase offset δ_ϕ. To this aim, we rewrite the likelihood (40) after relaxing the dependency of the LoS phase terms ϕ_n^{LoS} on the unknown UE position $\boldsymbol{p}$ and phase offset δ_ϕ, i.e., by considering a relaxed variable $\gamma_n^{\text{LoS}} = \alpha_n^{\text{LoS}} e^{j\phi_n^{\text{LoS}}}$ (with no phase-coherent structure) and treating $\{\gamma_n^{\text{LoS}}\}_{n=1}^N$ as unknown complex amplitudes. It is important to observe that we use this non-coherent relaxation only in the initial part of the derivation, whereas in the subsequent steps we will revert to the original phase-coherent structure. The non-coherent relaxation temporarily increases by $N-1$ the number of unknowns in $\breve{\boldsymbol{\eta}}$, due to an additional unknown phase term in $\boldsymbol{\phi}_n^{\text{RP}}$ for each RS n. We denote the new vector of unknown parameters as

$$\breve{\boldsymbol{\eta}}_{\text{ext}} = [\boldsymbol{p}^{\mathsf{T}}\ \delta_\tau\ \boldsymbol{\delta}_\phi^{\mathsf{T}}\ \boldsymbol{\gamma}_1^{\mathsf{T}}\ \cdots\ \boldsymbol{\gamma}_N^{\mathsf{T}}]^{\mathsf{T}} \in \mathbb{R}^{(D+1+N)\times 1} \times \mathbb{C}^{NL}, \tag{42}$$

with $\boldsymbol{\gamma}_n = [\gamma_n^{\text{LoS}}\ \gamma_{n,1}\ \cdots\ \gamma_{n,L-1}]^{\mathsf{T}}$ and, accordingly, rewrite (40) in matrix form as

$$\mathcal{L}^{\text{RML-NCP}}(\breve{\boldsymbol{\eta}}_{\text{ext}}) = \sum_{n=1}^{N} \Big\| \boldsymbol{y}'_n - \boldsymbol{C}'_n(\boldsymbol{p}, \delta_\tau)\boldsymbol{\gamma}_n \Big\|^2, \tag{43}$$

where the additional superscript NCP highlights the non-coherent processing of the signal paths, and

$$\boldsymbol{C}'_n(\boldsymbol{p}, \delta_\tau) \triangleq [\boldsymbol{c}'_{n,0}(\boldsymbol{p}, \delta_\tau)\ \cdots\ \boldsymbol{c}'_{n,L-1}(\boldsymbol{p}, \delta_\tau)]. \tag{44}$$

The relaxed UE localization and synchronization problem can be then recast as

$$\widehat{\breve{\boldsymbol{\eta}}}_{\text{ext}}^{\text{RML-NCP}} = \arg\min_{\breve{\boldsymbol{\eta}}_{\text{ext}}}\ \mathcal{L}(\breve{\boldsymbol{\eta}}_{\text{ext}}). \tag{45}$$

This problem is ancillary to the ultimate estimation of δ_ϕ: since (43) is a separable LS problem, the complex amplitudes can be estimated on a per-RS basis as a function of $\boldsymbol{p}$ and δ_τ as

$$\widehat{\boldsymbol{\gamma}}_n(\boldsymbol{p}, \delta_\tau) = (\boldsymbol{C}'_n(\boldsymbol{p}, \delta_\tau))^\dagger\, \boldsymbol{y}'_n \tag{46}$$

for $n = 1, \ldots, N$. From $\widehat{\boldsymbol{\gamma}}_n(\boldsymbol{p}, \delta_\tau)$, we pick only the LoS complex amplitudes and try to exploit their original structure $\widehat{\gamma}_n^{\text{LoS}} = \hat{\alpha}_n^{\text{LoS}} e^{j\hat{\phi}_n^{\text{LoS}}}$ to estimate the phase offset δ_ϕ. In fact, by inspecting (3), we observe that the relationship

$$\hat{\phi}_n^{\text{LoS}}(\boldsymbol{p}, \delta_\tau) = -2\pi f_{\text{c}} \tau_n^{\text{LoS}}(\boldsymbol{p}) + \delta_\phi(\boldsymbol{p}, \delta_\tau) \tag{47}$$

holds for each $n = 1, \ldots, N$. Notice that, having restored the coherent structure, we no longer need to estimate the unknown vector $\boldsymbol{\delta}_\phi$, but only a single scalar value δ_ϕ corresponding to the common phase offset between the UE and the entire network. This suggests that, conditioned on a tentative value of UE position (and of the clock offset for obtaining $\widehat{\boldsymbol{\gamma}}_n(\boldsymbol{p}, \delta_\tau)$), we can first apply a per-RS de-rotation by a complex factor as

$$\xi_n^{\text{LoS}}(\boldsymbol{p}, \delta_\tau) \triangleq \widehat{\gamma}_n^{\text{LoS}}(\boldsymbol{p}, \delta_\tau)\ e^{j2\pi f_{\text{c}} \tau_n^{\text{LoS}}(\boldsymbol{p})} \tag{48}$$

to compensate for the delay term in (3), leaving a dependency only on the sought δ_ϕ in ξ_n^{LoS}; then, all ξ_n^{LoS}'s can be summed and an estimate of the phase offset can be readily obtained as the argument of the resulting complex number, i.e.

$$\hat{\delta}_\phi^{\text{RML}}(\boldsymbol{p}, \delta_\tau) = \angle \sum_{n=1}^{N} \xi_n^{\text{LoS}}(\boldsymbol{p}, \delta_\tau). \tag{49}$$

The phase offset estimator is summarized in Algorithm 1.

Algorithm 1 Phase Offset Estimator

1: **Input:** $\{\boldsymbol{y}'_n\}_{n=1}^N$, $\boldsymbol{p} \in D$-dim. grid $\mathcal{G}_{\boldsymbol{p}}$, $\delta_\tau \in$ 1-dim. grid $\mathcal{G}_{\delta_\tau}$
2: Compute $\boldsymbol{C}'_n = [\boldsymbol{c}'_{n,0}\ \cdots\ \boldsymbol{c}'_{n,L-1}], \quad n = 1, \ldots, N$
3: Estimate $\widehat{\boldsymbol{\gamma}}_n = (\boldsymbol{C}'_n)^\dagger\, \boldsymbol{y}'_n, \quad n = 1, \ldots, N$
4: Compute τ_n^{LoS} via (5) $\quad n = 1, \ldots, N$
5: Compute $\xi_n^{\text{LoS}} = \widehat{\gamma}_n^{\text{LoS}} e^{j2\pi f_{\text{c}} \tau_n^{\text{LoS}}}, \quad n = 1, \ldots, N$
6: Estimate $\hat{\delta}_\phi^{\text{RML}} = \angle \sum_{n=1}^{N} \xi_n^{\text{LoS}}$

b) Estimation of UE Position and Clock Offset: At the first stage, we neglected phase coherence among all the RSs and proposed an approach to obtain a closed-form (conditional) estimate of the phase offset $\hat{\delta}_\phi$. Now, at the second stage, we plug such an estimate back into (40), where phase coherence among RSs is fully restored and follow the same ML steps as in (28)-(34) to obtain closed-form (conditional wrt $\boldsymbol{p}$ and δ_τ) estimates of $\boldsymbol{\alpha}^{\text{RP}}$ and $\boldsymbol{\phi}^{\text{RP}}$. Subsequently, the estimated vectors $\hat{\boldsymbol{\alpha}}^{\text{RP}}$ and $\hat{\boldsymbol{\phi}}^{\text{RP}}$, together with $\hat{\delta}_\phi$, can be substituted back into (40), yielding the compressed log-likelihood function

$$\mathcal{L}^{\text{RML}}(\boldsymbol{p},\delta_\tau)=\sum_{n=1}^{N}\left\|\boldsymbol{y}'_n-\breve{\boldsymbol{B}}_n(\boldsymbol{p},\delta_\tau)\mathring{\breve{\boldsymbol{B}}}_n^{\dagger}(\boldsymbol{p},\delta_\tau)\mathring{\boldsymbol{y}}'_n\right\|^2, \quad (50)$$

with

$$\breve{\boldsymbol{B}}_n \triangleq [e^{j\hat{\phi}_n^{\text{LoS}}}\boldsymbol{c}'(\theta_n^{\text{LoS}},\widetilde{\tau}_n^{\text{LoS}})\ \boldsymbol{c}'(\theta_{n,1}^{\text{RP}},\widetilde{\tau}_{n,1}^{\text{RP}})\ j\boldsymbol{c}'(\theta_{n,1}^{\text{RP}},\widetilde{\tau}_{n,1}^{\text{RP}})\ \cdots \\ \boldsymbol{c}'(\theta_{n,L-1}^{\text{RP}},\widetilde{\tau}_{n,L-1}^{\text{RP}})\ j\boldsymbol{c}'(\theta_{n,L-1}^{\text{RP}},\widetilde{\tau}_{n,L-1}^{\text{RP}})], \quad (51)$$

where $\hat{\phi}_n^{\text{LoS}}$ is given in (47) and, analogously to previous definitions in (38), $\mathring{\breve{\boldsymbol{B}}}_n=\begin{bmatrix}\breve{\boldsymbol{B}}_{n,R}\\ \breve{\boldsymbol{B}}_{n,I}\end{bmatrix}$ with $\breve{\boldsymbol{B}}_{n,R}=\Re\left\{\breve{\boldsymbol{B}}_n\right\}$, $\breve{\boldsymbol{B}}_{n,I}=\Im\left\{\breve{\boldsymbol{B}}_n\right\}$. Interestingly, as in (38), the dependencies left are only upon the parameters of interest $\boldsymbol{p}$ and δ_τ. As a result, the ultimate expression of the (approximate) UE position and clock offset estimator is

$$[\hat{\boldsymbol{p}}^{\text{RML}}\ \hat{\delta}_\tau^{\text{RML}}]=\arg\min_{\boldsymbol{p},\delta_\tau}\ \mathcal{L}^{\text{RML}}(\boldsymbol{p},\delta_\tau). \quad (52)$$

However, differently from (39), the approach proposed in this section further reduces the dimensionality of the estimation problem from $D+2+3J$ to only $D+1$.

The RML estimator is summarized in Algorithm 2.

Algorithm 2 RML for Initial UE Localization and Synchronization

Input: $\{\boldsymbol{y}'_n\}_{n=1}^N$, $\{\mathring{\boldsymbol{y}}'_n\}_{n=1}^N$, D-dim. grid $\mathcal{G}_{\boldsymbol{p}}$, 1-dim. grid $\mathcal{G}_{\delta_\tau}$
for $\underline{\boldsymbol{p}}\in\mathcal{G}_{\boldsymbol{p}}$ **do** $(n=1,\ldots,N;\ \ell=1,\ldots,L-1)$
  Compute τ_n^{LoS} via (5)
  Compute θ_n^{LoS} and $\theta_{n,\ell}^{\text{RP}}$ via (7)
  for $\underline{\delta_\tau}\in\mathcal{G}_{\delta_\tau}$ **do** $(n=1,\ldots,N;\ \ell=1,\ldots,L-1)$
    $\hat{\delta}_\phi^{\text{RML}}=\text{PhaseOffsetEstimator}(\{\boldsymbol{y}'_n\}_{n=1}^N,\underline{\boldsymbol{p}},\underline{\delta_\tau})$
    Compute $\hat{\phi}_n^{\text{LoS}}=-2\pi f_c\tau_n^{\text{LoS}}+\hat{\delta}_\phi^{\text{RML}}$
    Compute $\tilde{\tau}_n^{\text{LoS}}$ and $\tilde{\tau}_{n,\ell}^{\text{RP}}$ via (4)
    Compute $\breve{\boldsymbol{B}}_n$ via (51) and $\mathring{\breve{\boldsymbol{B}}}_n=\begin{bmatrix}\Re\{\breve{\boldsymbol{B}}_n\}\\ \Im\{\breve{\boldsymbol{B}}_n\}\end{bmatrix}$
    Compute $\mathcal{L}^{\text{RML}}(\underline{\boldsymbol{p}},\underline{\delta_\tau})=\sum_{n=1}^{N}\left\|\boldsymbol{y}'_n-\breve{\boldsymbol{B}}_n\mathring{\breve{\boldsymbol{B}}}_n^{\dagger}\mathring{\boldsymbol{y}}'_n\right\|^2$
  end for
end for
$[\hat{\boldsymbol{p}}^{\text{RML}}\ \hat{\delta}_\tau^{\text{RML}}]=\arg\min_{\underline{\boldsymbol{p}}\in\mathcal{G}_{\boldsymbol{p}},\underline{\delta_\tau}\in\mathcal{G}_{\delta_\tau}}\ \mathcal{L}^{\text{RML}}$

c) Low-Complexity Estimation of Clock Offset: To further reduce the dimensionality of the optimization problem in (52), we employ a low-complexity strategy to obtain a coarse estimate of δ_τ as a function of $\boldsymbol{p}$, consisting of the following steps. First, for each RS n, we estimate the pseudo-delay via IFFT over subcarriers and noncoherent integration over spatial (antennas) domain. Specifically, we switch from spatial-frequency domain to delay-spatial domain by computing $\boldsymbol{\mathcal{Y}}_n=\text{IFFT}(\boldsymbol{Y}_n^{\mathsf{T}})$ as the (per-column) IFFT-transformed delay-spatial observations over N_F points, where $\boldsymbol{Y}_n$ is the spatial-frequency observation at the n-th RS given in (13). This is followed by a noncoherent integration across the spatial domain (i.e., samples over the M antennas) and finding the index of the maximum element

$$\widehat{q}_n=\arg\max_q\left[\sum_{m=1}^{M}|[\boldsymbol{\mathcal{Y}}_n]_{q,m}|^2:0\le q\le N_F-1\right], \quad (53)$$

with $[\boldsymbol{\mathcal{Y}}_n]_{q,m}$ denoting the (q,m)-th entry of $\boldsymbol{\mathcal{Y}}_n$. Accordingly, a coarse estimate of the pseudo-delay $\widetilde{\tau}_n$ can be obtained by mapping the index $\hat{q}$ with the corresponding IFFT bin as

$$\widehat{\widetilde{\tau}}_n=\widehat{q}_n/(N_F\Delta f)\ . \quad (54)$$

Next, for a given trial position $\boldsymbol{p}$, the clock offset can be estimated by computing the difference between the pseudo-delay and the true delay at $\boldsymbol{p}$ based on (4), i.e.,

$$\widehat{\delta}_{\tau,n}(\boldsymbol{p})=\widehat{\widetilde{\tau}}_n-\frac{1}{\mathsf{c}}\|\boldsymbol{p}-\boldsymbol{p}_n^{\text{RS}}\|\ . \quad (55)$$

Finally, a coarse estimate of δ_τ can be obtained simply via averaging over the RSs:

$$\widehat{\delta}_\tau(\boldsymbol{p})=\frac{1}{N}\sum_{n=1}^{N}\widehat{\delta}_{\tau,n}(\boldsymbol{p})\ . \quad (56)$$

To determine the initialization point for (52), one can then perform a 3D search (2D for known height of UE) via

$$\hat{\boldsymbol{p}}^{\text{RML}}=\arg\min_{\boldsymbol{p}}\ \mathcal{L}^{\text{RML}}(\boldsymbol{p},\widehat{\delta}_\tau(\boldsymbol{p})), \quad (57)$$

yielding $(\hat{\boldsymbol{p}}^{\text{RML}},\widehat{\delta}_\tau(\hat{\boldsymbol{p}}^{\text{RML}}))$ as the initialization point for 4D numerical optimization in (52).

The RML estimator with reduced complexity is summarized in Algorithm 3.

Algorithm 3 RML for Initial UE Localization with Reduced Complexity Synchronization

Input: $\{\boldsymbol{y}'_n\}_{n=1}^N$, $\{\mathring{\boldsymbol{y}}'_n\}_{n=1}^N$, D-dim. grid $\mathcal{G}_{\boldsymbol{p}}$, 1-dim. grid $\mathcal{G}_{\delta_\tau}$
for $\underline{\boldsymbol{p}}\in\mathcal{G}_{\boldsymbol{p}}$ **do** $(n=1,\ldots,N;\ \ell=1,\ldots,L-1)$
  Estimate $\widehat{\delta}_\tau$ with low-complexity via IFFT using (53)-(56)
  Compute τ_n^{LoS} via (5)
  $\hat{\delta}_\phi^{\text{RML}}=\text{PhaseOffsetEstimator}(\{\boldsymbol{y}'_n\}_{n=1}^N,\underline{\boldsymbol{p}},\widehat{\delta}_\tau(\underline{\boldsymbol{p}}))$
  Compute $\hat{\phi}_n^{\text{LoS}}=-2\pi f_c\tau_n^{\text{LoS}}+\hat{\delta}_\phi^{\text{RML}}$
  Compute $\tilde{\tau}_n^{\text{LoS}}$ and $\tilde{\tau}_{n,\ell}^{\text{RP}}$ via (4)
  Compute θ_n^{LoS} and $\theta_{n,\ell}^{\text{RP}}$ via (7)
  Compute $\breve{\boldsymbol{B}}_n$ via (51) and $\mathring{\breve{\boldsymbol{B}}}_n=\begin{bmatrix}\Re\{\breve{\boldsymbol{B}}_n\}\\ \Im\{\breve{\boldsymbol{B}}_n\}\end{bmatrix}$
  Compute $\mathcal{L}^{\text{RML}}(\underline{\boldsymbol{p}})=\sum_{n=1}^{N}\left\|\boldsymbol{y}'_n-\breve{\boldsymbol{B}}_n\mathring{\breve{\boldsymbol{B}}}_n^{\dagger}\mathring{\boldsymbol{y}}'_n\right\|^2$
end for
$\hat{\boldsymbol{p}}^{\text{RML}}=\arg\min_{\underline{\boldsymbol{p}}\in\mathcal{G}_{\boldsymbol{p}}}\ \mathcal{L}^{\text{RML}}$
Compute $\widehat{\delta}_\tau^{\text{RML}}$ based on $\hat{\boldsymbol{p}}^{\text{RML}}$

2) Initial Mapping of Scatterers Positions: We devise an alternative strategy to obtain an initial estimate of all the SPs positions $\{\boldsymbol{p}_\iota^{\text{SP}}\}_{\iota=1}^J$, leveraging the initial (coarse) knowledge about UE position $\hat{\boldsymbol{p}}^{\text{RML}}$ and synchronization offsets $(\hat{\delta}_\tau^{\text{RML}},\hat{\delta}_\phi^{\text{RML}})$ gained using the previously-proposed algorithms. To this aim, we reconsider (44) and observe that the matrices $\boldsymbol{C}'_n(\boldsymbol{p},\delta_\tau)$, which contain the angular-delay response vectors $\boldsymbol{c}'_{n,\ell}(\boldsymbol{p},\delta_\tau)$, span a basis for the joint L-dimensional LoS and RPs space when evaluated for $\boldsymbol{p}=\hat{\boldsymbol{p}}^{\text{RML}}$ and $\delta_\tau=\hat{\delta}_\tau^{\text{RML}}$. Starting from these matrices, we propose an approach, hereafter referred to as *null-space transformation (NST)*, that leverages the subspace

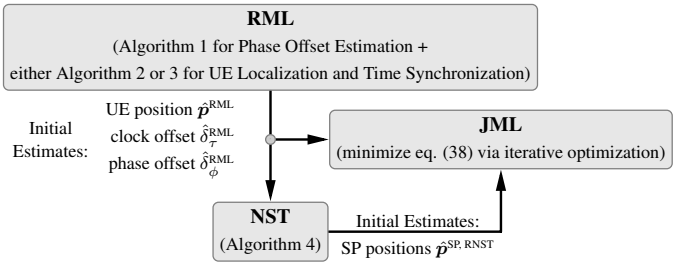

Fig. 3. Block diagram of the proposed three-stage algorithm.

orthogonal to the joint LoS/RPs space to approximately remove LoS and RPs paths from the received signals $\{\boldsymbol{y}'_n\}_{n=1}^N$. Specifically, we estimate a per-RS basis for the null space (kernel) of LoS and RPs vectors, using the coarse estimates of $\hat{\boldsymbol{p}}^{\text{RML}}$ and $\hat{\delta}_\tau^{\text{RML}}$, as follows

$$\boldsymbol{K}_n = \text{null}(\boldsymbol{C'}_n^{\mathsf{H}}(\hat{\boldsymbol{p}}^{\text{RML}}, \hat{\delta}_\tau^{\text{RML}})) \in \mathbb{C}^{MK \times MK-L}, \tag{58}$$

where $\text{null}(\cdot)$ denotes the operator returning a basis for the null space of the matrix argument. Then, for the resulting transformed version of the observables, $\boldsymbol{\zeta}_n = \boldsymbol{K}_n^{\mathsf{H}} \boldsymbol{y}'_n$, it holds

$$\boldsymbol{\zeta}_n = \sum_{\ell=0}^{L-1} \gamma_{n,\ell}^{\text{RP}} \underbrace{\boldsymbol{K}_n^{\mathsf{H}} \boldsymbol{c}'(\theta_{n,\ell}^{\text{RP}}, \widetilde{\tau}_{n,\ell}^{\text{RP}})}_{\approx \boldsymbol{0}} + \sum_{\iota=1}^{J} \gamma_{n,\iota}^{\text{SP}} \boldsymbol{K}_n^{\mathsf{H}} \boldsymbol{c}'(\theta_{n,\iota}^{\text{SP}}, \widetilde{\tau}_{n,\iota}^{\text{SP}}) + \boldsymbol{v}_n,$$

where $\boldsymbol{v}_n \triangleq \boldsymbol{K}_n^{\mathsf{H}} \boldsymbol{R}_n^{-1/2} \boldsymbol{w}_n$ and the approximation is obviously related to the fact that estimated projection matrices are used in place of the true ones. Based on $\boldsymbol{\zeta}_n$s, a reduced ML estimation problem can be formalized as

$$[\hat{\boldsymbol{p}}^{\text{SP, NST}} \ \hat{\boldsymbol{\gamma}}^{\text{SP, NST}}] = \arg \min_{\boldsymbol{p}^{\text{SP}}, \boldsymbol{\gamma}^{\text{SP}}} \ \mathcal{L}^{\text{NST}}(\boldsymbol{p}^{\text{SP}}, \boldsymbol{\gamma}^{\text{SP}}), \tag{59}$$

where $\boldsymbol{\gamma}^{\text{SP}} = [\boldsymbol{\gamma}_1^{\text{SP}\mathsf{T}} \ \cdots \ \boldsymbol{\gamma}_N^{\text{SP}\mathsf{T}}]^{\mathsf{T}}$, $\boldsymbol{\gamma}_n^{\text{SP}} = [\gamma_{n,1}^{\text{SP}} \ \cdots \ \gamma_{n,J}^{\text{SP}}]^{\mathsf{T}}$, and

$$\mathcal{L}^{\text{NST}}(\boldsymbol{p}^{\text{SP}}, \boldsymbol{\gamma}^{\text{SP}}) = \sum_{n=1}^{N} \left\| \boldsymbol{\zeta}'_n - \sum_{\iota=1}^{J} \gamma_{n,\iota}^{\text{SP}} \boldsymbol{g}'_n(\theta_{n,\iota}^{\text{SP}}, \widetilde{\tau}_{n,\iota}^{\text{SP}}) \right\|^2, \tag{60}$$

with $\boldsymbol{\zeta}'_n = (\boldsymbol{K}_n^{\mathsf{H}} \boldsymbol{K}_n)^{-1/2} \boldsymbol{\zeta}_n$ and $\boldsymbol{g}'_n(\theta_{n,\iota}^{\text{SP}}, \widetilde{\tau}_{n,\iota}^{\text{SP}}) = (\boldsymbol{K}_n^{\mathsf{H}} \boldsymbol{K}_n)^{-1/2} \boldsymbol{K}_n^{\mathsf{H}} \boldsymbol{c}'(\theta_{n,\iota}^{\text{SP}}, \widetilde{\tau}_{n,\iota}^{\text{SP}})$ resulting from the whitening of the noise, being $\mathbb{E}[\boldsymbol{v}_n \boldsymbol{v}_n^{\mathsf{H}}] = \boldsymbol{K}_n^{\mathsf{H}} \boldsymbol{K}_n$.[8] This estimation problem is still very complex, being $(3+N)J$-dimensional; to lower its complexity, we consider a relaxation that neglects part of the mixed terms in (60), i.e.,

$$\mathcal{L}^{\text{RNST}}(\boldsymbol{p}^{\text{SP}}, \boldsymbol{\gamma}^{\text{SP}}) = \sum_{\iota=1}^{J} \sum_{n=1}^{N} \left\| \boldsymbol{\zeta}'_n - \gamma_{n,\iota}^{\text{SP}} \boldsymbol{g}'_n(\theta_{n,\iota}^{\text{SP}}, \widetilde{\tau}_{n,\iota}^{\text{SP}}) \right\|^2. \tag{61}$$

This allows one to estimate each $\gamma_{n,\iota}^{\text{SP}}$ separately for all $\iota = 1, \ldots, J$, i.e., $\hat{\gamma}_{n,\iota}^{\text{SP, RNST}} = (\boldsymbol{g}'_n(\theta_{n,\iota}^{\text{SP}}, \widetilde{\tau}_{n,\iota}^{\text{SP}}))^{\dagger} \boldsymbol{\zeta}'_n$, and then perform a search for the J dominant dips (negative peaks) of $\sum_{n=1}^{N} \left\| \boldsymbol{\mathcal{P}}_{\boldsymbol{g}'_n}^{\perp} \boldsymbol{\zeta}'_n \right\|^2$, where $\boldsymbol{\mathcal{P}}_{\boldsymbol{A}}^{\perp} = \boldsymbol{I} - \boldsymbol{A}\boldsymbol{A}^{\dagger}$ is the projector onto the orthogonal complement to the subspace spanned by the columns of $\boldsymbol{A}$. The resulting estimates $\hat{\boldsymbol{p}}^{\text{SP, RNST}}$ are thus obtained through a procedure with remarkably lower complexity, amounting to a single three-dimensional search.

The NST estimator is summarized in Algorithm 4.

Fig. 3 depicts a diagram of the main blocks of the proposed three-stage approach, illustrating how they interconnect and flow sequentially.

[8]Notice that if $\boldsymbol{K}_n$ is selected as an orthonormal basis, $\boldsymbol{K}_n^{\mathsf{H}} \boldsymbol{K}_n = \boldsymbol{I}$ hence pre-whitening is not necessary (and $\boldsymbol{\zeta}'_n = \boldsymbol{\zeta}_n$).

Algorithm 4 NST for Initial Mapping of Scatterers Positions

Input: $\{\boldsymbol{y}'_n\}_{n=1}^N$, $\hat{\boldsymbol{p}}^{\text{RML}}$, $\hat{\delta}_\tau^{\text{RML}}$, $\hat{\delta}_\phi^{\text{RML}}(\hat{\boldsymbol{p}}^{\text{RML}}, \hat{\delta}_\tau^{\text{RML}})$, 3-dim. grid $\mathcal{G}_{\mathfrak{s}}$
$(n = 1, \ldots, N)$
Compute $\boldsymbol{C'}_n^{\mathsf{H}} = [\boldsymbol{c}'_{n,0}(\hat{\boldsymbol{p}}^{\text{RML}}, \hat{\delta}_\tau^{\text{RML}}) \ \cdots \ \boldsymbol{c}'_{n,L-1}(\hat{\boldsymbol{p}}^{\text{RML}}, \hat{\delta}_\tau^{\text{RML}})]^{\mathsf{H}}$
Compute $\boldsymbol{K}_n = \text{null}(\boldsymbol{C'}_n^{\mathsf{H}})$
Compute $\boldsymbol{\zeta}'_n = (\boldsymbol{K}_n^{\mathsf{H}} \boldsymbol{K}_n)^{-1/2} \boldsymbol{K}_n^{\mathsf{H}} \boldsymbol{y}'_n$
for $\mathfrak{s} \in \mathcal{G}_{\mathfrak{s}}$ **do** $(n = 1, \ldots, N)$
  Compute θ_n^{SP} and $\tilde{\tau}_n^{\text{SP}}$ via (4) and (7) using $\hat{\boldsymbol{p}}^{\text{RML}}$ and $\hat{\delta}_\tau^{\text{RML}}$
  Compute $\boldsymbol{g}'_n(\theta_n^{\text{SP}}, \tilde{\tau}_n^{\text{SP}}) = (\boldsymbol{K}_n^{\mathsf{H}} \boldsymbol{K}_n)^{-1/2} \boldsymbol{K}_n^{\mathsf{H}} \boldsymbol{c}'(\theta_n^{\text{SP}}, \tilde{\tau}_n^{\text{SP}})$
  Compute $\boldsymbol{\mathcal{P}}_{\boldsymbol{g}'_n}^{\perp} = \boldsymbol{I} - \dfrac{\boldsymbol{g}'_n(\theta_n^{\text{SP}}, \tilde{\tau}_n^{\text{SP}}) \boldsymbol{g}'^{\mathsf{H}}_n(\theta_n^{\text{SP}}, \tilde{\tau}_n^{\text{SP}})}{\|\boldsymbol{g}'_n(\theta_n^{\text{SP}}, \tilde{\tau}_n^{\text{SP}})\|^2}$
  Compute $\mathcal{L}^{\text{RNST}}(\underline{\mathfrak{s}}) = \sum_{n=1}^{N} \|\boldsymbol{\mathcal{P}}_{\boldsymbol{g}'_n}^{\perp} \boldsymbol{\zeta}'_n\|^2$
end for
Select J dominant dips of $\mathcal{L}^{\text{RNST}}$ to obtain $\hat{\boldsymbol{p}}^{\text{SP, RNST}}$

C. Computational Complexity Analysis

In this section, we discuss the computational complexity of the joint localization, synchronization and mapping algorithm proposed in Sec. V-B alongside that of the plain JML estimator (39) in Sec. V-A.

1) Complexity of the Plain JML Estimator (39) *in Sec. V-A:* In asymptotic terms, we find that the complexity of executing the multi-dimensional optimization required by (39) scales as

$$O(Q^{D_{\text{tot}}} NMK(L+J)), \tag{62}$$

where $D_{\text{tot}} = D + 2 + 3J$ represents the total dimension of the estimation problem in (39), Q refers to the number of evaluation points for each dimension (i.e., p_x coordinate and p_y coordinate of the UE position, clock offset δ_τ, phase offset δ_ϕ and SP positions $\boldsymbol{p}^{\text{SP}}$), taken to be the same for all the dimensions for clarity, and $D = 2$ or $D = 3$ indicates the number of unknown UE position coordinates.

2) Complexity of the Proposed Low-Complexity Algorithm in Sec. V-B: Breaking down the different stages outlined in the proposed algorithm in Sec. V-B, we identify that the overall asymptotic complexity is captured by the sum of three terms

$$O(NMN_F \log N_F) + O(Q^2 NMKL) + O(Q^3 NMKJ). \tag{63}$$

Here, $O(NMN_F \log N_F)$ accounts for the complexity involved in computing the IFFT of each column of $\boldsymbol{Y}_n^{\mathsf{T}} \in \mathbb{C}^{K \times M}$ in (53) for $n = 1, \ldots, N$, where $\boldsymbol{Y}_n$ is the spatial-frequency observation matrix at RS n, defined in (13), and N_F is the IFFT size. In addition, $O(Q^2 NMKL)$ reflects the complexity of the two-dimensional optimization required to derive the initial estimate of the UE position $\hat{\boldsymbol{p}}^{\text{RML}}$ according to (57), which utilizes the LoS+RP model involving L paths per RS. Finally, $O(Q^3 NMKJ)$ indicates the complexity involved in executing the three-dimensional optimization in (61) to determine the locations of the J SPs at the final step of the proposed algorithm.

3) Complexity Comparison: Given that the minimum number of points needed for computing the IFFT roughly matches the length of the vectors involved, that is, $N_F \approx K$, it becomes clear that the last term, $O(Q^3 NMKJ)$, primarily determines the overall complexity of the proposed algorithm, given in (63). This term reflects the complexity of the three-dimensional search necessary to determine the locations of the SPs. In this respect, the proposed low-complexity algorithm is able to reduce the complexity required by the plain JML estimator, given in (62): in fact, the latter grows with $Q^{D_{\text{tot}}}$, which for

practical value of the parameter can be as large as ten or more, while the proposed algorithm keeps a cubic cost in Q.

VI. Cramér-Rao Lower Bound

We derive the CRLB for joint localization, synchronization and mapping with distributed RSs, i.e.[9]

$$\mathbb{E}_{\boldsymbol{\eta}}\left[(\hat{\boldsymbol{\eta}}-\boldsymbol{\eta})(\hat{\boldsymbol{\eta}}-\boldsymbol{\eta})^{\mathsf{T}}\right] \succeq \boldsymbol{J}^{-1}, \tag{64}$$

where $\boldsymbol{J}$ is the Fisher information matrix (FIM) for the global parameter vector $\boldsymbol{\eta}$. We assume that each RS n contributes independent information on $\boldsymbol{\eta}$, i.e., assuming identical DMC[10] and noise statistics, the FIM for the parameter vector $\boldsymbol{\eta}$ is

$$\boldsymbol{J} = \sum_{n=0}^{N-1} \boldsymbol{T}_n \boldsymbol{J}_{\boldsymbol{\eta}^{\text{ch}}}^{(n)} \boldsymbol{T}_n^{\mathsf{T}} \quad \in \mathbb{R}^{\mathcal{D}_{\text{g}}\times\mathcal{D}_{\text{g}}}, \tag{65}$$

which is the sum of the local channel FIMs $\boldsymbol{J}_{\boldsymbol{\eta}^{\text{ch}}}^{(n)}$ contributed by all N RSs and propagated via the Jacobian matrices $\boldsymbol{T}_n \in \mathbb{R}^{\mathcal{D}_{\text{g}}\times\mathcal{D}_{\text{ch}}}$ from local channel parameter level to global parameter level. Depending on the considered level of synchronization, the dimension $\mathcal{D}_{\text{g}}$ of the global parameter vector $\boldsymbol{\eta}$ changes according to (22). The dimension $\mathcal{D}_{\text{ch}}$ of the local per-RS channel parameter vector $\boldsymbol{\eta}_n^{\text{ch}}$ stays constant in both the NCP and the CP case. It is defined as

$$\boldsymbol{\eta}_n^{\text{ch}} = \Big[\underbrace{\boldsymbol{\theta}_n^{\text{RP}\,\mathsf{T}}\boldsymbol{\theta}_n^{\text{SP}\,\mathsf{T}}}_{\boldsymbol{\theta}_n^{\mathsf{T}}} \; \underbrace{\widetilde{\boldsymbol{\tau}}_n^{\text{RP}\,\mathsf{T}}\widetilde{\boldsymbol{\tau}}_n^{\text{SP}\,\mathsf{T}}}_{\widetilde{\boldsymbol{\tau}}_n^{\mathsf{T}}} \; \underbrace{\boldsymbol{\phi}_n^{\text{RP}\,\mathsf{T}}\boldsymbol{\phi}_n^{\text{SP}\,\mathsf{T}}}_{\boldsymbol{\phi}_n^{\mathsf{T}}} \; \underbrace{\boldsymbol{\alpha}_n^{\text{RP}\,\mathsf{T}}\boldsymbol{\alpha}_n^{\text{SP}\,\mathsf{T}}}_{\boldsymbol{\alpha}_n^{\mathsf{T}}}\Big]^{\mathsf{T}} \tag{66}$$

and captures the stacked channel parameters for all components κ impinging at RS n hence its dimension is $\mathcal{D}_{\text{ch}} \triangleq 4\,N_{\text{c}}$. The elements of the local channel FIM $\boldsymbol{J}_{\boldsymbol{\eta}^{\text{ch}}}^{(n)} \in \mathbb{R}^{\mathcal{D}_{\text{ch}}\times\mathcal{D}_{\text{ch}}}$ are defined as [45, Sec. 15.7]

$$\left[\boldsymbol{J}_{\boldsymbol{\eta}^{\text{ch}}}^{(n)}\right]_{i,j} = 2\Re\left\{\frac{\partial\boldsymbol{\mu}_{n,\kappa}^{\mathsf{H}}}{\partial[\boldsymbol{\eta}_n^{\text{ch}}]_i}\boldsymbol{R}_n^{-1}\frac{\partial\boldsymbol{\mu}_{n,\kappa}}{\partial[\boldsymbol{\eta}_n^{\text{ch}}]_j}\right\}, \tag{67}$$

where $\boldsymbol{\mu}_{n,\kappa} = \alpha_{n,\kappa}e^{j\phi_{n,\kappa}}\boldsymbol{c}(\theta_{n,\kappa},\widetilde{\tau}_{n,\kappa})$ denotes the noise-free signal for each component κ encompassing the LoS, all RPs, and all SPs. The individual entries of the local channel FIM $\boldsymbol{J}_{\boldsymbol{\eta}^{\text{ch}}}^{(n)}$ from (67) can be found in Supplementary Material S-IV-A. While the dimension of the channel FIM $\boldsymbol{J}_{\boldsymbol{\eta}^{\text{ch}}}^{(n)}$ stays constant in the CP and NCP cases, the dimension of the Jacobian matrices changes. The Jacobian matrices are

$$\boldsymbol{T}_n = \frac{\partial\boldsymbol{\eta}_n^{\text{ch}\,\mathsf{T}}}{\partial\boldsymbol{\eta}} = \begin{bmatrix} \boldsymbol{P}_n^{\theta} & \boldsymbol{P}_n^{\widetilde{\tau}} & \boldsymbol{P}_n^{\phi} & \boldsymbol{0} \\ \boldsymbol{0} & \boldsymbol{C}_n^{\widetilde{\tau}} & \boldsymbol{C}_n^{\phi} & \boldsymbol{0} \\ \boldsymbol{P}_{\text{SP},n}^{\theta} & \boldsymbol{P}_{\text{SP},n}^{\widetilde{\tau}} & \boldsymbol{P}_{\text{SP},n}^{\phi} & \boldsymbol{0} \\ \boldsymbol{0} & \boldsymbol{0} & \boldsymbol{A}_{\phi,n} & \boldsymbol{0} \\ \boldsymbol{0} & \boldsymbol{0} & \boldsymbol{0} & \boldsymbol{A}_{\alpha,n} \end{bmatrix} \in \mathbb{R}^{\mathcal{D}_{\text{g}}\times\mathcal{D}_{\text{ch}}}, \tag{68}$$

with individual submatrices defined in Supplementary Material S-IV-B. Note that the presented CRLB represents a lower bound on the estimation error of $\hat{\boldsymbol{\eta}}$ under the assumption of the correct detection and association of all components.

We aim to compute the position error bound (PEB) and clock error bounds (CEBs) for the parameters of interest. This can be done either by computing the complete CRLB matrix through inverting the large FIM $\boldsymbol{J}$ in (65), or computing the equivalent FIM (EFIM) by partitioning $\boldsymbol{\eta}$ in parameters of interest $\boldsymbol{\eta}_{\text{w}}$ and nuisance parameters $\boldsymbol{\eta}_{\text{u}}$ as indicated in (20). In the latter case, block-partitioning the FIM

$$\boldsymbol{J} = \begin{bmatrix} \boldsymbol{J}_{\boldsymbol{\eta}_{\text{w}}\boldsymbol{\eta}_{\text{w}}} & \boldsymbol{J}_{\boldsymbol{\eta}_{\text{w}}\boldsymbol{\eta}_{\text{u}}} \\ \boldsymbol{J}_{\boldsymbol{\eta}_{\text{w}}\boldsymbol{\eta}_{\text{u}}}^{\mathsf{T}} & \boldsymbol{J}_{\boldsymbol{\eta}_{\text{u}}\boldsymbol{\eta}_{\text{u}}} \end{bmatrix}, \tag{69}$$

the EFIM is computed as $\boldsymbol{J}_{\text{e}} = \boldsymbol{J}_{\boldsymbol{\eta}_{\text{w}}\boldsymbol{\eta}_{\text{w}}} - \boldsymbol{J}_{\boldsymbol{\eta}_{\text{w}}\boldsymbol{\eta}_{\text{u}}}\boldsymbol{J}_{\boldsymbol{\eta}_{\text{u}}\boldsymbol{\eta}_{\text{u}}}^{-1}\boldsymbol{J}_{\boldsymbol{\eta}_{\text{w}}\boldsymbol{\eta}_{\text{u}}}^{\mathsf{T}}$ [46] from which the PEB for $\boldsymbol{p}$ with dimensions D is obtained as

$$\mathcal{P} = \sqrt{\text{tr}\left([\boldsymbol{J}_{\text{e}}^{-1}]_{1:D,1:D}\right)} \tag{70}$$

and the CEBs are the clock offset error bound for δ_τ

$$\mathcal{C}_\tau = \sqrt{[\boldsymbol{J}_{\text{e}}^{-1}]_{D+1,D+1}} \tag{71}$$

and the phase offset error bound is defined as

$$\mathcal{C}_\phi = \sqrt{\text{tr}\left([\boldsymbol{J}_{\text{e}}^{-1}]_{D+2:D+1+N_{\text{ph}},D+2:D+1+N_{\text{ph}}}\right)}, \tag{72}$$

where N_{ph} indicates the number of phase parameters which is $N_{\text{ph}}=1$ or $N_{\text{ph}}=N$ for coherent (CP) and non-coherent processing (NCP), respectively. For SP j we define the corresponding SP-PEB as

$$\mathcal{P}_{\text{SP},j} = \sqrt{\text{tr}\left([\boldsymbol{J}_{\text{e}}^{-1}]_{\mathcal{S}+(j-1)D_{\text{SP}}:\mathcal{S}+jD_{\text{SP}},\mathcal{S}+(j-1)D_{\text{SP}}:\mathcal{S}+jD_{\text{SP}}}\right)}, \tag{73}$$

where $\mathcal{S} = D+2+N_{\text{ph}}$ and $D_{\text{SP}}=3$ is the dimension of the estimated SP position.

VII. Simulation Results

In Fig. 1, we provide an illustration of the considered scenario with simulation parameters from Table I. There are $N=4$ RSs mounted in a room with $L=4$ walls[11] (▭) and $J=2$ SPs (●). Clearly, the performance of this system (in terms of both positioning and mapping) can be naturally improved by increasing N and/or M. In this respect, our choice to consider a moderate parameter configuration is intended to demonstrate that the proposed method effectively leverages the phase-coherent ELAA setup even with a reduced number of antennas per RS. This choice, in turn, also reduces system complexity, making the approach more practical.

As to the UE (▫), it is located in the center of the room and transmits uplink pilots. The uplink pilots take paths via the LoS (- - -), paths via RPs (- - -), and paths via SPs (- - -) which impinge on the RSs. The positions of RPs (⋄) are computed geometrically according to Supplementary Material S-II-A. The walls in the scenario depicted in Fig. 1 are assumed to be made of *concrete* with typical relative permeability $\mu_{\text{r}}=1$, relative permittivity $\epsilon_{\text{r}}=6$ [48], and conductivity $\sigma_1 = 1\times10^{-2}\,\text{S/m}$ [49], [50]. We assume linearly polarized antennas at both the RSs and UE with polarization vectors $\boldsymbol{\rho}_n^{\text{RS}} = \boldsymbol{\rho}^{\text{UE}} = [0\ 0\ 1]^{\mathsf{T}}$ aligned with the z-axis.

A. Fundamental Performance Limits

For the scenario in Fig. 1 we evaluate the PEB as a function of the bandwidth B, varying the antennas M and hence the aperture per RS given a constant antenna spacing d.

[9] $\boldsymbol{X} \succeq \boldsymbol{0}$ denotes a positive semidefinite matrix [45].

[10] Apart from the onset time τ_{d}, which is coupled with the LoS delay τ_n^{LoS}.

[11] Based on our choice of antenna polarizations, we omit modeling a floor and ceiling as the reflection coefficients $R_{n,\ell}^{\parallel}$ in (S9) will be generally much lower than $R_{n,\ell}^{\perp}$ in (S10) [47, cf. Fig. 1.14].

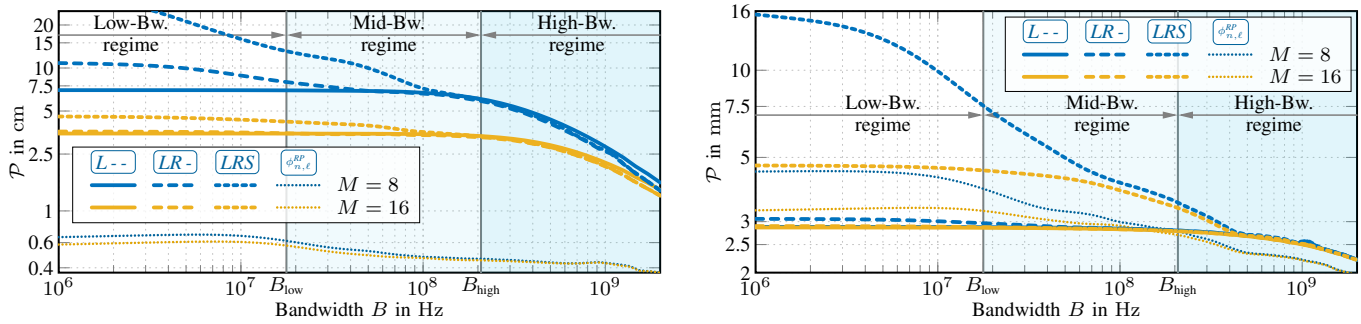

(a) NCP (b) CP

Fig. 4. The NCP PEB $\mathcal{P}$ in cm (a) and CP PEB (b) in mm as a function of bandwidth B, varying the number of antennas M at an SDNR $= 0$ dB. We compare the LoS-only case, with LoS and RPs, and with LoS, RPs, and SPs. The latter is augmented with a scenario assuming known RP phases $\phi^{\text{RP}}_{n,\ell}$.

TABLE I
LIST OF DEFAULT SIMULATION PARAMETERS IF NOT STATED OTHERWISE.

Variable	Symbol	Value	Unit
Carrier frequency	f_{c}	3.5	GHz
RS antenna spacing	d	$\lambda/2.1$	m
No. subcarriers	K	20	-
No. antennas	M	16	-
DNR	DNR	0	dB
SDNR	SDNR	0	dB
UE position	$\boldsymbol{p}$	$[3.03\ 2.87\ 1]^{\mathsf{T}}$	m
RS height	$\boldsymbol{p}^{\text{RS}}_n$	2.75	m
SP1 position	$\boldsymbol{p}^{\text{SP}}_1$	$[2\ 2.2\ 0.5]^{\mathsf{T}}$	m
SP2 position	$\boldsymbol{p}^{\text{SP}}_2$	$[4\ 2\ 1.5]^{\mathsf{T}}$	m
SP1 radius	r^{SP}_1	19.56	cm
SP2 radius	r^{SP}_2	17.57	cm
Rel. permittivity	ϵ_{r}	6	-
Rel. permeability	μ_{r}	1	-
Conductivity	σ_1	1×10^{-2}	S/m

NCP *Bandwidth and Aperture Sweep*

Fig. 4(a) depicts the NCP PEB for the cases of LoS-only (L - -), LoS and RPs (LR -) and LoS, RPs, and SPs (LRS) propagation, and for LRS case with known RP phases ($\phi^{RP}_{n,\ell}$).

For L - - the PEB remains almost flat for bandwidths $B < B_{\text{high}}$. This is because noncoherently positioning the UE with distributed RSs is dominated by angular information $[\boldsymbol{J}_{\theta,\theta}]^{(n)}_{\kappa,\kappa'}$ (cf. Table S-I) until the bandwidth becomes large enough ($B \geq B_{\text{high}}$) so delay information starts to dominate the PEB. We call this the *high-bandwidth regime*. Below this regime, *path overlap* costs information [51] in the LR - and LRS cases w.r.t. the LoS-only case through large off-diagonal elements in $\boldsymbol{J}^{(n)}_{\boldsymbol{\eta}^{\text{ch}}}$. We define the *low-bandwidth regime* as the region $B \leq B_{\text{low}}$, where the LoS overlaps with RPs in both the angular and delay domains. The *mid-bandwidth regime* $B_{\text{low}} < B < B_{\text{high}}$ is characterized by a bandwidth large enough to separate the LoS from RPs in the delay domain. We next derive simple expressions for B_{low} and B_{high} that capture the characteristics of the bandwidth regimes.

Assuming a white covariance matrix $\boldsymbol{R}_n$ the proportionality $[\boldsymbol{J}_{\theta,\theta}]^{(n)}_{\kappa,\kappa'} \propto 2\Re\{\boldsymbol{b}^{\mathsf{H}}(\overline{\tau}_{\text{RP}})\boldsymbol{b}(\overline{\tau}_{\text{LoS}})/K\}$ holds, where we define the average LoS delay as $\overline{\tau}_{\text{LoS}} := \frac{1}{N}\sum_{n=1}^{N}\tau^{\text{LoS}}_n$, and the average RP delay as $\overline{\tau}_{\text{RP}} := \frac{1}{N(L-1)}\sum_{n=1}^{N}\sum_{\ell=1}^{L-1}\tau^{\text{RP}}_{n,\ell}$. For $[\boldsymbol{J}_{\theta,\theta}]^{(n)}_{\kappa,\kappa'}$, this expression corresponds to the delay-domain RP overlap cost relative to the delay-domain LoS component information. It can be further expressed as $\frac{1}{K}\sum_{k=0}^{K-1}\cos(2\pi\Delta_f k\Delta\tau)$, with $\Delta\tau := \overline{\tau}_{\text{RP}} - \overline{\tau}_{\text{LoS}}$, and is plotted in Fig. 5(a) (——). Using $\Delta_f \triangleq \frac{B}{K}$, we approximate this result as $\frac{1}{2}\left(1+\cos(2\pi B\frac{K-1}{K}\Delta\tau)\right)$ which is indicated by the dashed curve (- - -) in Fig. 5(a). We choose the bandwidth threshold between the low and mid-bandwidth regimes (dotted line) to lie where this path overlap cost has dropped to $F = -3\,\text{dB} = \frac{1}{\sqrt{2}}$ which results in

$$B_{\text{low}} = \frac{K\ \arccos(2F-1)}{2\pi\Delta\tau(K-1)} \approx 17.78\,\text{MHz}\,. \tag{74}$$

The high-bandwidth regime is characterized by the delay information $[\boldsymbol{J}_{\tilde{\tau},\tilde{\tau}}]^{(n)}_{1,1'} \propto \|\dot{\boldsymbol{b}}(\tau^{\text{LoS}}_n)\|^2$ dominating the PEB over the angular information $[\boldsymbol{J}_{\theta,\theta}]^{(n)}_{1,1'} \propto \|\dot{\boldsymbol{a}}(\theta^{\text{LoS}}_n)\|^2$. Note that $\dot{\boldsymbol{b}} = \frac{\partial \boldsymbol{b}}{\partial \tau}$ from (S15) and $\dot{\boldsymbol{a}} = \frac{\partial \boldsymbol{a}}{\partial \theta}$ from (S14). The Jacobians that map to position $\boldsymbol{p}$ have the proportionalities $\boldsymbol{P}^{\theta}_n \propto \frac{1}{c\overline{\tau}^{\text{LoS}}_n}$ and $\boldsymbol{P}^{\tilde{\tau}}_n \propto \frac{1}{c}$. Equating $\frac{1}{c^2\overline{\tau}^2_{\text{LoS}}}\|\dot{\boldsymbol{a}}(0)\|^2 = \frac{1}{c^2}\|\dot{\boldsymbol{b}}(\tau^{\text{LoS}}_n)\|^2$ and abbreviating $S_M \triangleq \sum_{m=-\frac{M-1}{2}}^{\frac{M-1}{2}} m^2 = \frac{M(M^2-1)}{12}$ and $S_K \triangleq \sum_{k=0}^{K-1} k^2 = \frac{2K^3-3K^2+K}{6}$, we solve for B contained in $\dot{\boldsymbol{b}}$ to compute the high bandwidth regime threshold (for $M = 12$) as

$$B_{\text{high}} = \frac{Kd}{\overline{\tau}_{\text{LoS}}\lambda}\sqrt{\frac{S_M}{S_K}} \approx 207.9\,\text{MHz}\,. \tag{75}$$

Following the discussion of our RP channel model in Sec. S-II-B, the case $\phi^{RP}_{n,\ell}$ assumes known RP component phases $\phi^{\text{RP}}_{n,\ell}$. Although this is rather unrealistic in practice, we present the respective curves in Fig. 4(a) to illustrate the substantial theoretical gains in positioning accuracy achievable by exploiting (perfect) knowledge of per-RS component phases. This effectively transforms the angle or delay-based NCP positioning into carrier-phase-based positioning.

CP *Bandwidth and Aperture Sweep*

Fig. 4(b) depicts the PEB $\mathcal{P}$ in the CP setting for the three different multipath cases. Having knowledge of the clock phases at distributed RSs allows the phase-coherent processing of the impinging components. While our channel model in Sec. III assumes that each RP and each SP introduces an unknown phase that varies for every RS n, there are N LoS components impinging at the infrastructure which only need to be used to estimate a single[12] phase offset δ_ϕ to the UE (common to all RSs). Hence the remaining phases of $N-1$ LoS components contribute a significant amount of information about the UE position due to the high curvature of the likelihood function around the true position $\boldsymbol{p}$ but come at the price of a harder estimation problem due to its shape,

[12]Note that in the NCP case, N LoS component phases need to be used to estimate N phase offsets contained in $\boldsymbol{\delta}_\phi$ which costs the information they could have contributed on the UE position.

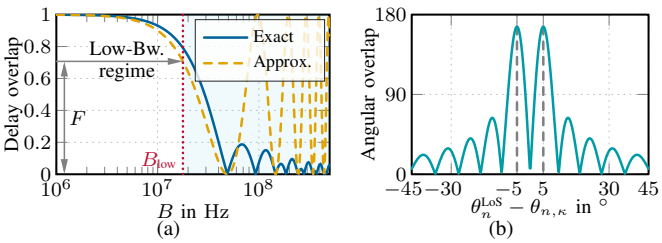

Fig. 5. Path overlap in the delay domain causes large correlations in $[\boldsymbol{J}_{\theta,\theta}]^{(n)}_{\kappa,\kappa'}$. Angular overlap causes large correlations in $[\boldsymbol{J}_{\theta,\phi}]^{(n)}_{0,\kappa'}$.

which we demonstrate in Sec. VII-B2 (cf. Fig. 10(b)) [52]. While the array spacing of each individual RS satisfies the Nyquist rate, phase-coherent processing among multiple RSs effectively turns the RS infrastructure into a large aliased array, implying a multimodal likelihood function which complicates the estimation problem. However, the CRLB gives solely insight into the estimation accuracy achievable around the *true* parameters [53]. While the PEB is generally much lower in the CP case than in the NCP case (note the vertical axis scaling in Fig. 4(a) and Fig. 4(b)), we again observe a performance degradation in the presence of path overlap with RPs and SPs, due to the coupling term depicted in Fig. 5(a). The PEB remains almost flat in the LoS-only case L--. In the LR,- case, path overlap with RPs causes slight PEB degradation, while in the LRS case, overlap with SPs leads to significantly greater degradation. In the $\phi^{RP}_{n,\ell}$ case, the gain of knowing RP phases is marginal as the PEB is dominated by information from LoS phases.

NCP *Spatial Sweep*

The impact of angular path overlap gets more conceivable when evaluating the PEB $\mathcal{P}$ spatially in the form of heatmaps. We show a heatmap for $\mathcal{P}$ in the low-bandwidth regime in Fig. 6. The "checked pattern" is caused by the information contributed by the carrier phase. It is observable that there are "white stripes" connecting the centers of RSs with SPs and RPs that are located at straight lines originating at RSs and orthogonally intersecting wall surfaces. These straight lines indicate positions of the UE, where the LoS and respective SP or RP components overlap completely in the *angular domain*. A positioning performance degradation due to path overlap is observable just outside these straight lines, where components start to separate in the angular domain. This can be explained by larger off-diagonal elements (i.e., coupling terms) $[\boldsymbol{J}_{\theta,\phi}]^{(n)}_{0,\kappa'}$ of the LoS AoAs and NLoS component phases in the channel FIM. Assuming a white DMC covariance matrix, we would have $[\boldsymbol{J}_{\theta,\phi}]^{(n)}_{0,\kappa'} \propto \Re\left\{j\frac{\partial \boldsymbol{a}^{\mathsf{H}}(\theta_n^{\text{LoS}})}{\partial \theta_n^{\text{LoS}}}\boldsymbol{a}(\theta_{n,\kappa})\right\}$, a coupling term depicted in Fig. 5(b) (——) for $\theta_{n,\kappa} = 0$ and varying θ_n^{LoS}. A "white stripe" corresponds to the null where both angles are equal. It is surrounded by two larger lobes. In room corners, the path overlap of the LoS with RPs in both the angular- and delay domains causes a strong performance degradation.

Apart from the room corners the impact of path overlap with the RPs is resolved in the mid-bandwidth regime, as they are now well separated from the LoS in the *delay domain*. While the RPs are located at greater distances s.t. they arrive "later" at the RSs in the *delay domain* than the SPs, which are following the LoS much closer in the delay domain. Hence, the impact of path overlap with SPs is still visible in the mid-bandwidth regime as is well-observable in Fig. 7.

In the high-bandwidth regime, the bandwidth is large enough to ensure all components are well separated in the delay domain. The path overlap is largely resolved and the PEB is spatially smooth. Delay information dominates in this bandwidth regime and improves the PEB as can be seen from Fig. 8.

B. *Performance of Algorithms*

In this part, we evaluate the performance of the proposed joint localization, synchronization and mapping algorithms from Sec. V with phase-coherent RSs CP. We consider a UE located at $\boldsymbol{p} = [3.0297\ 2.8735\ 1]^{\mathsf{T}}\,\text{m}$ (an off-grid value to exclude any advantage for the algorithm during grid-based optimization), with clock offset $\delta_\tau = 16.66\,\text{ns}$ corresponding to $5\,\text{m}$ in range, and phase offset $\delta_\phi = 45°$. To lower the computation time, we assume known height of the UE and consider a single SP located at $\boldsymbol{p}_t^{\text{SP}} = [2.5\ 3.5\ 1.7]^{\mathsf{T}}\,\text{m}$. The bandwidth, number of RSs, and number of antennas per RS are set to $B = 10\,\text{MHz}$, $N = 4$ and $M = 8$, respectively. Performance obtained through 100 independent Monte Carlo trials is shown for *(i)* the RML estimator in (52), which operates with reduced complexity as outlined in Sec. V-B, and *(ii)* the optimal JML in (39) initialized by the RML, RML-NCP in (45) and RNST in (61), as described in Sec. V-A.[13]

1) RMSE Analysis: Fig. 9 depicts the root-mean-squared error (RMSE) performance of the considered estimators, along with the corresponding CRLB, for estimation of the UE location in Fig. 9(a) and clock offset in Fig. 9(b).[14] It is apparent that the overall accuracy for the UE position is in the sub-meter regime and rapidly reaches centimeter-level values, even at intermediate SDNR levels, before asymptotically decreasing to sub-millimeter accuracy towards high SDNR levels. More specifically, the proposed RML is able to achieve remarkable performance, with RMSE equal to a few centimeters already at 5 dB SDNR, despite its low complexity. This, in turn, provides satisfactory initializations for the JML estimator, which attains the CRLB already at 15 dB SDNR for both the UE location, PEB CP in Fig. 9(a), and clock offset, CEB in Fig. 9(b). Towards low SDNR levels, both the RML and JML approach the NCP PEB, with the JML estimators deviation from the CP PEB coinciding with the deviation from the CEB in Fig. 9(b). This can be attributed to the increased distortion of the estimated LoS phases at low SDNR levels, resulting in increasing phase offset estimation errors, thus inhibiting fully coherent performance. The same trend can be observed in the phase offset estimation performance, whose analysis is postponed to Sec. VII-B3 where the full empirical distribution is reported.

Note that this CEB is predominantly affected by the delay resolution. In fact, only the delay domain maps (via the Jacobian matrices $\boldsymbol{C}_n^{\tilde{\tau}}$) directly to the clock offset, though it also "couples" with the UE position $\boldsymbol{p}$ through off-diagonal FIM elements. Therefore, while the CEB is indirectly improved in the CP case as a result of a more accurate UE position

[13] More specifically, *(i)* refers to coarse estimation of UE position $\hat{\boldsymbol{p}}^{\text{RML}}$ and clock offset $\widehat{\delta}_\tau(\hat{\boldsymbol{p}}^{\text{RML}})$ via (57) and (56), respectively, using coarse estimate of phase offset $\widehat{\delta}_\phi^{\text{RML}}(\hat{\boldsymbol{p}}^{\text{RML}}, \widehat{\delta}_\tau(\hat{\boldsymbol{p}}^{\text{RML}}))$ via (49); *(ii)* uses the same estimation and, in addition, coarse SP position estimates $\hat{\boldsymbol{p}}^{\text{SP, RNST}}$ via (61) to initialize the optimal JML that considers the true ML cost function (39).

[14] In computing the RMSE, error values have been cleaned up from a few outliers (via the standard inter-quartile range method). These are due to the very spiky landscape of minima in the UE location coordinates, as will be discussed in the next subsection.

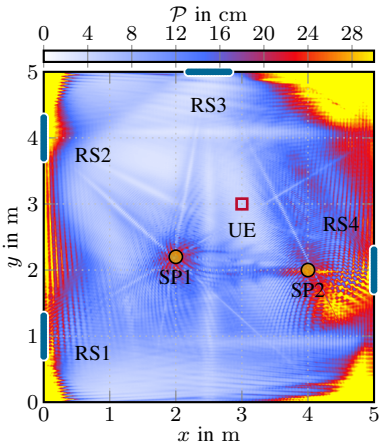

Fig. 6. PEB in the low-bandwidth regime: At $B = 3$ MHz, path overlap of LoS with SPs and RPs degrades positioning accuracy, particularly in room corners. Angular information dominates the PEB.

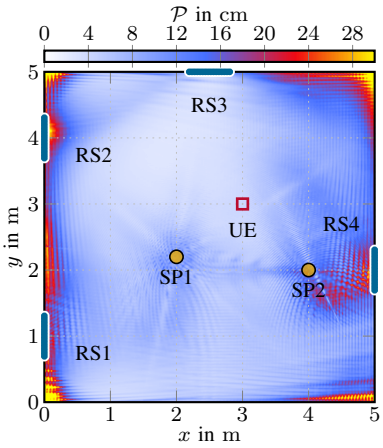

Fig. 7. PEB in the mid-bandwidth regime: At $B = 30$ MHz, path overlap with the RPs is resolved but path overlap with SPs still degrades positioning accuracy. Angular information dominates the PEB.

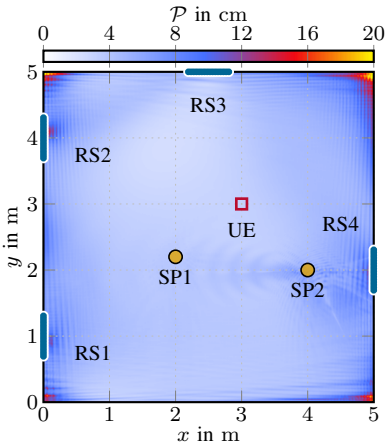

Fig. 8. PEB in the high-bandwidth regime: At $B = 300$ MHz, the path overlap of the LoS with the both the RPs and the SPs is resolved. Delay information dominates the PEB.

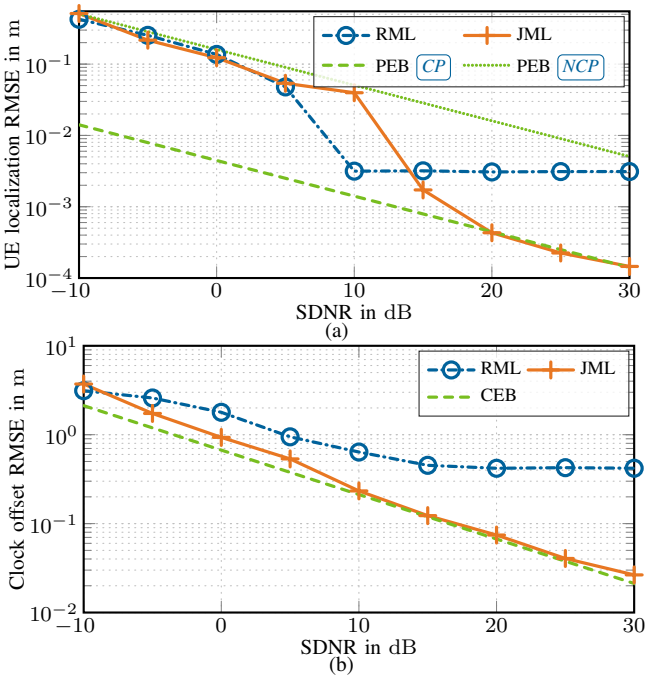

Fig. 9. RMSE on the estimation of (a) UE location $\boldsymbol{p}$ and (b) clock offset δ_τ, achieved by RML and JML along with CRLBs as a function of SDNR.

estimation, clock estimation improves only slightly, being the PEB dominated not by clock but by angular information in the NCP case, and by phase information in the CP case (in the low- and mid-bandwidth regimes). Consequently, the CEB curves for clock offset almost coincide in the NCP and CP cases, hence only the latter is plotted in Fig. 9(b).

As to the performance plateau observed for values of the SDNR ≥ 10 dB, it should be attributed to the fact that the RML estimator is derived by neglecting the paths that originate from SPs, as per (40). Consequently, as typical in the case of misspecified or mismatched estimators (e.g., [54], [55]), the estimator's performance is fundamentally limited by its mismatch to the full signal model (which instead includes LoS, RPs, and SPs). In summary, the results demonstrate the effectiveness of the JML in utilizing all the available information from the coherent processing, significantly improving upon the initial estimates provided by the RML, hence achieving accurate localization and synchronization.

2) Cost Functions Analysis: To illustrate the impact of phase coherence on the behavior of cost functions employed in the proposed estimation algorithms, we report in Fig. 10 and Fig. 11 examples of both noncoherent and coherent cost functions relative to the UE position. As seen from Fig. 10, the RML-NCP cost function (43) NCP exhibits a smooth surface whereas the RML cost function (50) CP leads to a spiky profile with numerous local minima near the true UE position, despite being a relaxation of the JML. Indeed, spikiness results from leveraging LoS carrier phase information in (3) in CP, which links the UE position $\boldsymbol{p}$ in (5) to the LoS phase in (3) through the term $2\pi f_c \tau_{n,\ell}^{\mathrm{RP}}$; hence, the coherent cost function RML, and *a fortiori* the JML, show wavelength-level fluctuations (i.e., 0.086 m).

In contrast, when phase coherence is ignored as in the RML-NCP (43), the NCP cost depends on $\boldsymbol{p}$ only through the subcarrier-dependent phase shifts in (2), resulting in fluctuations on the level of inverse of bandwidth (i.e., 30 m). To further highlight the distinctions observed between NCP and CP processing, we also show the 1D cost functions relative to x-coordinate of UE position in Fig. 11, with and without the presence of SP, which reveal the effect of incorporating carrier phase information into position estimation. In summary, CP enables high-accuracy estimates via the use of a cost function highly sensitive to small position perturbations, which strongly motivates the proposed multi-step approach in Sec. V. The drawback is that, in a few cases, the search routine may fail in locating the correct minimum, so leading to error outliers that, in fact, have been removed in the RMSE computations discussed above. Nonetheless, in the following, we provide a deeper error analysis by providing the complete empirical cumulative distribution function (ECDF).

3) Empirical Cumulative Distribution Function Analysis: In Fig. 12(a) and Fig. 12(b), we present the ECDF curves for the estimation errors of the UE location $\boldsymbol{p}$ and the clock offset δ_τ, achieved by the RML and JML estimators at two different SDNR levels. Such curves confirm the same findings obtained by analyzing the RMSE, but provide more insights on the error distribution. We observe in particular that RML and JML provide cm-level and mm-level accuracy most of the times, respectively, but some outliers in estimation of the UE location are also present due to the spiky nature of the cost functions, as discussed above (cf. Fig. 10 and Fig. 11). For the same reason, the JML may not outperform (or even perform slightly worse than) the RML, though this mostly happens

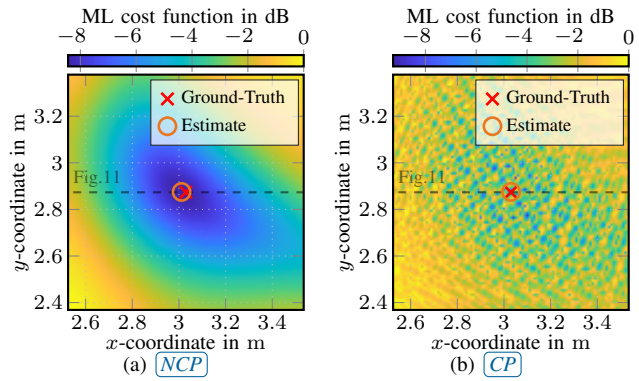

Fig. 10. ML cost functions with respect to the x- and y-coordinates of UE position in (a) NCP (43) and (b) CP (50) at SDNR = 20 dB. The cutting plane shown in Fig. 11 is indicated with a dashed line.

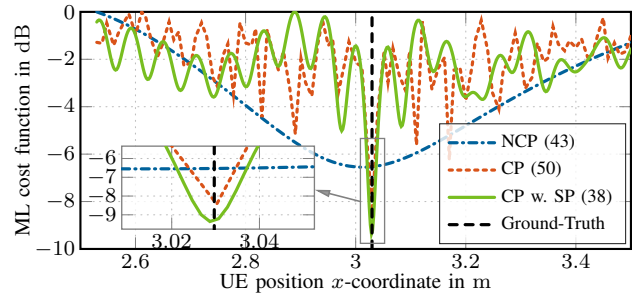

Fig. 11. ML cost functions with respect to the x-coordinate of UE position in NCP (43), CP (50) and CP (with SP) (38) at SDNR = 20 dB.

at very low SDNR. In contrast, clock offset errors have a smoother ECDF profile, because the dependence of (50) and (38) on δ_τ is only through subcarrier-level phase progressions, as apparent from (2) and (4). As to the phase offset, the ECDF reported in Fig. 12(c) shows that the RML performs very close to the JML for low SDNR, while providing improvement for higher SDNR.

To complete the analysis, we also report the ECDF curves for the mapping, i.e., the SP location errors. Fig. 12(d) confirms that, also for such variables, the proposed JML and RML provide satisfactory performance, yielding sub-meter accuracy at high SDNRs. Since the SP location estimation does not rely on carrier phase information (due to unknown scattering-induced phase shift as seen from (3)), the JML cost function exhibits a smooth behavior with respect to SP location, resulting in outlier-free ECDF curves. This also enables JML to outperform RML in most cases, similar to the clock offset estimation.

Finally, we highlight that the proposed algorithms directly extend to the estimation of multiple SPs, by searching for multiple dominant dips (negative peaks) in the RNST cost function (61). Performance results confirm the same findings as above (figures are omitted due to lack of space).

4) Complexity Analysis: To corroborate the theoretical analysis, we have also carried out simulations to evaluate the computational time of the algorithms. We report in Fig. 13(a) the average runtime normalized with respect to the plain JML, for $Q = 7$. We can show the comparison only for Q not larger than this low value since the formidable complexity of the plain JML with grid searches makes the runtime explode immediately. It is observed that the proposed RML-based algorithm drastically reduces the runtime by more than 95% for $Q = 7$. In agreement with the asymptotic analysis presented

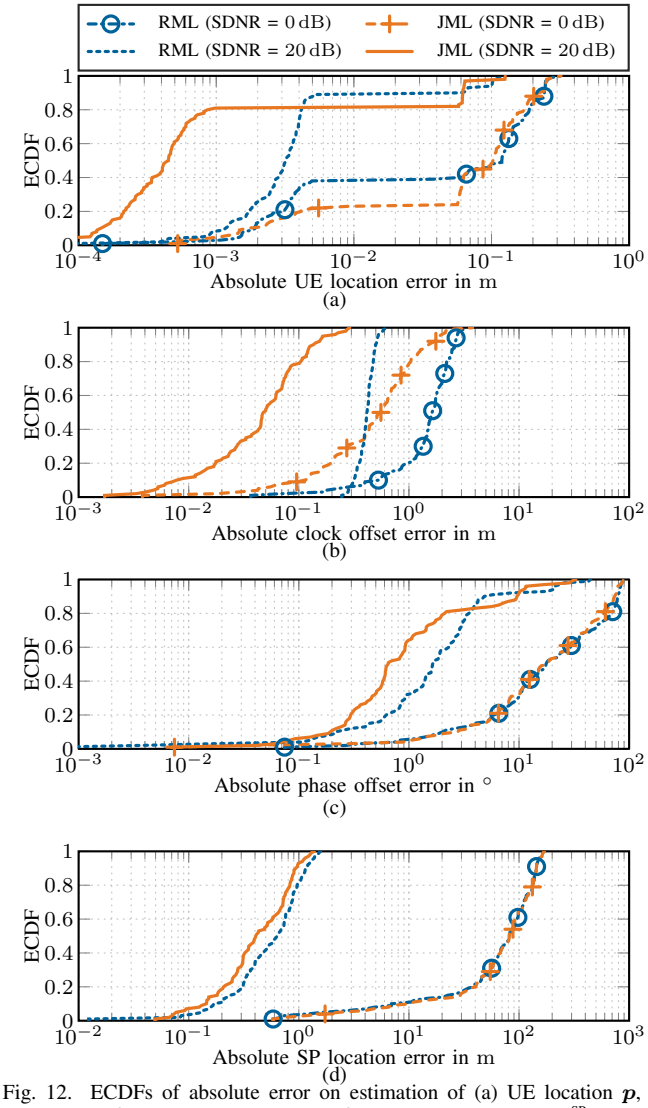

Fig. 12. ECDFs of absolute error on estimation of (a) UE location $\boldsymbol{p}$, (b) clock offset δ_τ, (c) phase offset error δ_ϕ, and (d) SP location $\boldsymbol{p}_t^{\text{SP}}$, achieved by RML and JML for two SDNR levels.

in (62) and (63), such a gap non-linearly widens very quickly with Q. Fig. 13(a) also shows as inset the breakdown of the proposed algorithm complexity, in terms of its three stages (RML, NST, and iterative JML): it is apparent that for low Q the iterative stage takes most of the time. For larger values of Q, instead, the asymptotic analysis in (63) suggests that the first two stages (RML and NST) dominate the overall complexity. This is confirmed by the results reported for $Q = 50$ in Fig. 13(b), which shows the relative comparison between the two variants of the proposed three-stage algorithm, namely with either 3D grid search or IFFT based clock offset estimation. We remark that, as discussed, computation of the plain JML for this more realistic value of Q is not feasible. Remarkably, as visible in the figure, the proposed low-complexity IFFT-based clock offset estimation in the RML stage yields a further significant improvement, which amounts to about 33% of the overall cost, thus making the algorithm suitable for practical applications.

VIII. Conclusion

In this work, we have studied the potential of ELAA systems implemented as distributed RS networks, particularly for joint localization, synchronization, and mapping in sub-6 GHz uplink channels. To correctly capture the complex

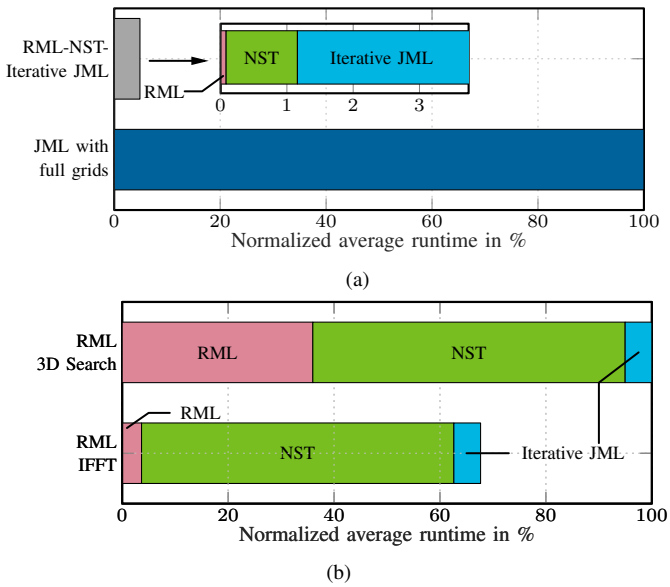

Fig. 13. Average runtime relative comparison between the (a) plain JML vs. proposed three-stage algorithm and (b) proposed algorithm with either 3D grid search or IFFT based clock offset estimation in the RML stage.

propagation characteristics of these environments, including specular reflections from walls, scattering from objects, and diffuse multipath, we first presented a detailed generative model able to describe signals and channels over the distributed RS network. We then formulated the joint localization, synchronization and mapping problem, leveraging the near-field effects of distributed RSs in both the presence or absence of phase synchronization between the UE and the RS network.

Through a comprehensive Fisher information analysis, we showed that a noncoherently operating, distributed RS network mainly relies on AoA information in the low and mid-bandwidth regimes, where path overlap with multipath components impairs accuracy. In the high bandwidth regime, it relies instead on delay information. On the other hand, a coherently operating, distributed RS network operates through carrier-phase based positioning where large performance gains come at the cost of a more involved estimation problem.

We also derived the ML estimator for joint localization, synchronization, and mapping and showed that, through a suitable decomposition, optimal (in ML sense) estimates of the channel amplitudes can be obtained in closed form. This allowed us to significantly reduce the dimensionality of the estimation problem and end up with a log-likelihood function depending only on the parameters of interest. To overcome the still-too-high dimensionality of the problem, we then devised a three-stage algorithm that suitably decouples the estimation of UE position and synchronization parameters from the SP position parameters, providing their initial estimates at a significantly reduced cost. Simulation analyses demonstrated the effectiveness of the proposed methods in capitalizing on near-field effects and a distributed network of phase-coherent RSs to achieve satisfactory localization, synchronization, and mapping performance. Specifically, a simple deployment with 4 RSs, each equipped with an 8-element ULA, proved sufficient for our algorithms to provide high-quality localization, offering submeter level accuracy even at low SDNR values and mm-level accuracy already at mid SDNR values.

We demonstrated that accurate environment information can enable a noncoherent RS network to process the LoS and SMCs (that is, RPs and SPs) coherently at each RS. While large performance gains can be made as a result of this coherent combination, knowledge of position and orientation of specular surfaces is required. Relaxing this assumption constitutes a possible future research direction.

Finally, incorporating model order estimation into the proposed algorithm would enhance its practical applicability. As such, this is a further possible future research direction, to better handle complex environments with unknown or dynamically changing model orders.

REFERENCES

[1] S. Dang *et al.*, "What should 6G be?" *Nature Electronics*, vol. 3, no. 1, pp. 20–29, 2020.

[2] S. Chen *et al.*, "Beam-space multiplexing: Practice, theory, and trends, from 4G TD-LTE, 5G, to 6G and beyond," *IEEE Wireless Commun.*, vol. 27, no. 2, pp. 162–172, 2020.

[3] Z. Wang *et al.*, "A tutorial on extremely large-scale MIMO for 6G: Fundamentals, signal processing, and applications," *IEEE Commun. Surveys Tuts.*, 2024.

[4] W. Hong *et al.*, "The role of millimeter-wave technologies in 5G/6G wireless communications," *IEEE Journal of Microwaves*, vol. 1, no. 1, pp. 101–122, 2021.

[5] K. Rikkinen *et al.*, "THz radio communication: Link budget analysis toward 6G," *IEEE Commun. Mag.*, vol. 58, no. 11, pp. 22–27, 2020.

[6] J. Lee *et al.*, "MIMO technologies in 3GPP LTE and LTE-advanced," *EURASIP Journal on wireless communications and networking*, vol. 2009, pp. 1–10, 2009.

[7] J. An *et al.*, "Near-field communications: Research advances, potential, and challenges," *IEEE Wireless Commun.*, vol. 31, no. 3, pp. 100–107, 2024.

[8] H. Chen *et al.*, "6G localization and sensing in the near field: Features, opportunities, and challenges," *IEEE Wireless Commun.*, 2024.

[9] J. A. del Peral-Rosado *et al.*, "Survey of cellular mobile radio localization methods: From 1G to 5G," *IEEE Commun. Surveys Tuts.*, vol. 20, no. 2, pp. 1124–1148, 2017.

[10] X. Li *et al.*, "Massive MIMO-based localization and mapping exploiting phase information of multipath components," *IEEE Trans. Wireless Commun.*, vol. 18, no. 9, pp. 4254–4267, 2019.

[11] A. Behravan *et al.*, "Positioning and sensing in 6G: Gaps, challenges, and opportunities," *IEEE Veh. Technol. Mag.*, vol. 18, no. 1, pp. 40–48, 2022.

[12] A. Elzanaty *et al.*, "Near and far field model mismatch: Implications on 6G communications, localization, and sensing," *IEEE Internet of Things Magazine*, vol. 7, no. 5, pp. 120–126, 2024.

[13] T. Wild *et al.*, "6G integrated sensing and communication: From vision to realization," in *2023 20th European Radar Conference (EuRAD)*. IEEE, 2023, pp. 355–358.

[14] G. Interdonato *et al.*, "Ubiquitous cell-free massive MIMO communications," *EURASIP Journal on Wireless Communications and Networking*, vol. 2019, no. 1, pp. 1–13, 2019.

[15] Z. H. Shaik *et al.*, "MMSE-optimal sequential processing for cell-free massive MIMO with radio stripes," *IEEE Trans. Commun.*, vol. 69, no. 11, pp. 7775–7789, 2021.

[16] A. K. Mishra *et al.*, "Millimeter wave and radio stripe: A prospective wireless technology for 6G and beyond networks," in *2021 Smart Technologies, Communication and Robotics (STCR)*, 2021, pp. 1–3.

[17] O. L. A. López *et al.*, "Massive MIMO with radio stripes for indoor wireless energy transfer," *IEEE Transactions on Wireless Communications*, vol. 21, no. 9, pp. 7088–7104, 2022.

[18] P. Frenger *et al.*, "Improved antenna arrangement for distributed massive MIMO," International Patent WO 2018/103 897 A1, June 14, 2018.

[19] D. Dardari *et al.*, "LOS/NLOS near-field localization with a large reconfigurable intelligent surface," *IEEE Trans. Wireless Commun.*, vol. 21, no. 6, pp. 4282–4294, 2022.

[20] N. BniLam *et al.*, "Synchronization of multiple independent subarray antennas: An application for angle of arrival estimation," *IEEE Trans. Antennas Propag.*, vol. 67, no. 2, pp. 1223–1232, 2019.

[21] M. D. Zoltowski *et al.*, "Closed-form 2-D angle estimation with rectangular arrays in element space or beamspace via unitary ESPRIT," *IEEE Trans. Signal Process.*, vol. 44, no. 2, pp. 316–328, 1996.

[22] A. Elzanaty *et al.*, "Towards 6G holographic localization: Enabling technologies and perspectives," *IEEE Internet of Things Magazine*, 2023.

[23] Q. Yang *et al.*, "Near-field localization with dynamic metasurface antennas," in *2023 IEEE International Conference on Acoustics, Speech and Signal Processing (ICASSP)*. IEEE, 2023, pp. 1–5.

[24] Z. Lu *et al.*, "Near-field localization and channel reconstruction for ELAA systems," *IEEE Trans. Wireless Commun.*, 2023.

[25] C. Ozturk *et al.*, "RIS-aided near-field localization under phase-dependent amplitude variations," *IEEE Trans. Wireless Commun.*, vol. 22, no. 8, pp. 5550–5566, 2023.

[26] M. Rahal *et al.*, "RIS-enabled NLoS near-field joint position and velocity estimation under user mobility," *IEEE J. Sel. Topics Signal Process.*, 2024.

[27] N. Vukmirović *et al.*, "Direct wideband coherent localization by distributed antenna arrays," *Sensors*, vol. 19, no. 20, p. 4582, 2019.

[28] ——, "Position estimation with a millimeter-wave massive MIMO system based on distributed steerable phased antenna arrays," *EURASIP journal on advances in signal processing*, vol. 2018, pp. 1–17, 2018.

[29] ——, "Performance limits of direct wideband coherent 3D localization in distributed massive MIMO systems," *Sensors*, vol. 21, no. 10, 2021.

[30] Y. Sun *et al.*, "Three dimensional source localization using arrival angles from linear arrays: Analytical investigation and optimal solution," *IEEE Trans. Signal Process.*, vol. 70, pp. 1864–1879, 2022.

[31] A. Fascista *et al.*, "Uplink joint positioning and synchronization in cell-free deployments with radio stripes," in *2023 IEEE International Conference on Communications Workshops (ICC Workshops)*. IEEE, 2023, pp. 1330–1336.

[32] M. E. Leinonen *et al.*, "Initial radio models and analysis towards ultra-high data rate links in 6G," Hexa-X project Deliverable D2.2, 2021. [Online]. Available: https://hexa-x.eu/deliverables/

[33] J. Nikonowicz *et al.*, "Indoor positioning in 5G-advanced: Challenges and solution toward centimeter-level accuracy with carrier phase enhancements," *IEEE Wireless Commun.*, 2024.

[34] A. Richter, "Estimation of radio channel parameters: Models and algorithms," Ph.D. dissertation, Technische Universität Ilmenau, Germany, February 2005.

[35] O. Edfors *et al.*, "Initial assessment of architectures and hardware resources for a RadioWeaves infrastructure," Jan. 2022. [Online]. Available: https://doi.org/10.5281/zenodo.5938909

[36] S. Grebien *et al.*, "Super-resolution estimation of UWB channels including the dense component – An SBL-inspired approach," *IEEE Trans. Wireless Commun.*, Feb. 2024.

[37] A. Venus *et al.*, "A graph-based algorithm for robust sequential localization exploiting multipath for obstructed-LOS-bias mitigation," *IEEE Trans. Wireless Commun.*, vol. 23, no. 2, pp. 1068–1084, June 2023.

[38] O. L. A. López *et al.*, "Massive MIMO with radio stripes for indoor wireless energy transfer," *IEEE Trans. Wireless Commun.*, pp. 1–1, 2022.

[39] "Discussion of potential techniques for NR positioning," in *CATT, 3GPP R1-1810532*, 2018.

[40] L. Wielandner *et al.*, "MIMO multipath-based SLAM for non-ideal reflective surfaces," in *Proc. Fusion-2024*, Venice, Italy, Jul. 2024, pp. 1–8.

[41] E. Leitinger *et al.*, "Data fusion for multipath-based SLAM: Combining information from multiple propagation paths," *IEEE Trans. Signal Process.*, vol. 71, pp. 4011–4028, Sep. 2023.

[42] X. Li *et al.*, "A belief propagation algorithm for multipath-based SLAM with multiple map features: A mmWave MIMO application," in *2024 IEEE International Conference on Communications Workshops (ICC Workshops)*, 2024, pp. 269–275.

[43] E. Tanghe *et al.*, "Experimental analysis of dense multipath components in an industrial environment," *IEEE Trans. Antennas Propag.*, vol. 62, no. 7, pp. 3797–3805, 2014.

[44] M. Wax *et al.*, "Detection of signals by information theoretic criteria," *IEEE Trans. Acoust., Speech, Signal Process.*, vol. 33, no. 2, pp. 387–392, 1985.

[45] S. M. Kay, *Fundamentals of Statistical Signal Processing: Estimation Theory*. Upper Saddle River, NJ: Prentice Hall, 1993.

[46] H. L. Van Trees, *Optimum Array Processing: Part IV of Detection, Estimation, and Modulation Theory*, ser. Detection, Estimation, and Modulation Theory. John Wiley & Sons, Inc., 2002.

[47] D. M. Pozar, *Microwave Engineering*, 4th ed. Wiley, 2012.

[48] M.-K. Olkkonen *et al.*, "Complex permittivity of concrete in the frequency range 0.8 to 12 GHz," in *2013 7th European Conference on Antennas and Propagation (EuCAP)*, 2013, pp. 3319–3321.

[49] L. Pîslaru-Dănescu *et al.*, "New concept of measurement apparatus for the in situ electrical resistivity of concrete structures," in *2013 8th International Symposium on Advanced Topics in Electrical Engineering (ATEE)*, 2013, pp. 1–6.

[50] V. Degli-Esposti *et al.*, "Measurement and modelling of scattering from buildings," *IEEE Trans. Antennas Propag.*, vol. 55, no. 1, pp. 143–153, 2007.

[51] Y. Shen *et al.*, "Effect of path-overlap on localization accuracy in dense multipath environments," in *2008 IEEE International Conference on Communications (ICC)*, 2008, pp. 4197–4202.

[52] H. Wymeersch *et al.*, "Fundamental performance bounds for carrier phase positioning in cellular networks," in *2023 IEEE Global Communications Conference (GLOBECOM)*, 2023, pp. 7478–7483.

[53] T. Wilding *et al.*, "Single-anchor, multipath-assisted indoor positioning with aliased antenna arrays (invited paper)," in *2018 52nd Asilomar Conference on Signals, Systems, and Computers*, 2018, pp. 525–531.

[54] C. Ozturk *et al.*, "RIS-aided localization under pixel failures," *IEEE Transactions on Wireless Communications*, vol. 23, no. 8, pp. 8314–8329, 2024.

[55] P. Zheng *et al.*, "Misspecified Cramér-Rao bound of RIS-aided localization under geometry mismatch," in *ICASSP 2023 - 2023 IEEE International Conference on Acoustics, Speech and Signal Processing (ICASSP)*, 2023, pp. 1–5.